Microvascular endothelial cells engulf myelin debris and contribute to macrophage recruitment and fibrotic scar formation after neural injury

Tian Zhou[1,2]*, Yiming Zheng[2*#], Li Sun[2], Smaranda Ruxandra Badea[3], Yuanhu Jin[2], Yang Liu[2,4,], Alyssa J. Rolfe[2], Haitao Sun[3,5], Xi Wang[6], Zhijian Cheng[2], Zhaoshuai Huang[2,7], Na Zhao[2,7], Xin Sun[8], Jinhua Li[9], Jianqing Fan[10], Choogon Lee[2], Timothy L. Megraw[2], Wutian Wu[8,11,12], Guixue Wang[1#], Yi Ren[2,4,7#]

* Tian Zhou and Yiming Zheng contribute equally to this study.

1. Key Laboratory of Biorheological Science & Technology, Ministry of Education, State & Local Joint Engineering Laboratory for Vascular Implants, College of Bioengineering, Chongqing University, Chongqing 400044, China.

2. Department of Biomedical Sciences, Florida State University College of Medicine, Tallahassee, FL, 32306, USA.

3. School of Biomedical Sciences, Li Ka Shing Faculty of Medicine, The University of Hong Kong, Hong Kong SAR, 999077, China.

4. Department of Immunology, Guizhou Medical University, Guiyang 550025, China.

5. Department of Neurosurgery, Zhujiang Hospital, Southern Medical University, Guangzhou 510282, China.

6. Institute of Neurosciences, the Fourth Military Medical University, Xi'an 710032, China.

7. Institute of Inflammation and Diseases, the First Affiliated Hospital of Wenzhou Medical University, Wenzhou, China.

8. Guangdong-Hong Kong-Macau Institute of CNS Regeneration, Jinan University, Guangzhou 510632, China.

9. Department of Anatomy and Developmental Biology, Monash University, Clayton, Victoria 3800, Australia.

10. Statistical Laboratory, Princeton University, NJ, 08540, USA.

11. Re-Stem Biotechnology Co., Ltd, Suzhou 215100, China

12. School of Biomedical Sciences, The University of Hong Kong, Hong Kong SAR, 999077, China

#Corresponding authors:

Dr. Yi Ren

Department of Biomedical Sciences

Florida State University College of Medicine

1115 West Street, Tallahassee, FL, 32306, USA

Email: yi.ren@med.fsu.edu

Or

Yiming Zheng

Department of Biomedical Sciences

Florida State University College of Medicine

1115 West Street, Tallahassee, FL, 32306, USA

Email: yz13@my.fsu.edu

Or

Dr. Guixue Wang

Key Laboratory of Biorheological Science & Technology, Ministry of Education

State & Local Joint Engineering Laboratory for Vascular Implants

College of Bioengineering

Chongqing University

Chongqing 400044, China

Email: wanggx@cqu.edu.cn

Abstract

The clearance of damaged myelin sheaths is critical to ensure functional recovery from neural injury. Here we show a previously unidentified role for microvessels and their lining endothelial cells (ECs) in engulfing myelin debris in spinal cord injury (SCI) and experimental autoimmune encephalomyelitis (EAE). We demonstrate that IgG opsonization of myelin debris is required for its effective engulfment by ECs and that the autophagy-lysosome pathway is crucial for the degradation of engulfed myelin debris. We further show that ECs exert critical functions beyond myelin clearance to promote progression of demyelination disorders by regulating macrophage infiltration, pathologic angiogenesis and fibrosis in both SCI and EAE. Unexpectedly, myelin debris engulfment induces the endothelial-to-mesenchymal transition, a process that confers upon EC the ability to stimulate the endothelial-derived production of fibrotic components. Overall, our study demonstrates that the processing of myelin debris through the autophagy-lysosome pathway promotes inflammation, angiogenesis, and fibrotic scar formation.

Keywords: spinal cord injury (SCI); experimental autoimmune encephalomyelitis (EAE); multiple sclerosis; myelin debris; endothelial cells; macrophages; autophagy; angiogenesis; inflammation; fibrosis; endothelial-to-mesenchymal transition (endoMT)

Introduction

A contusive spinal cord injury (SCI) induces acute mechanical compression of myelin sheath and causes prominent demyelination, a characteristics that is also well documented in multiple sclerosis (MS) and other demyelinating diseases. The myelin loss, neuronal damage, and spinal microvasculature disruption following SCI trigger a cascade of secondary pathological processes including inflammation, glial and fibrotic scar formation that prevent tissue regeneration and functional recovery[1,2,3]. Myelin debris, which is generated from the breakdown of myelin sheaths immediately after SCI, persists in the injury site and contributes to regeneration failure because myelin debris contains molecules that potently inhibit axon regeneration[4, 5] and remyelination[6, 7]. Moreover, myelin debris is actively involved in inflammatory responses during SCI progression[8-10]. Therefore, clearance of myelin debris from the injury site is critical for axon regeneration, remyelination and resolution of inflammation.

Myelin debris is cleared mainly by "professional" phagocytes such as bone marrow-derived macrophages (BMDMϕ) and resident microglia[10-12]. However, BMDMϕ are not significantly recruited to the injury site until one week after SCI[10] and microglia are generally absent from the lesion epicenter[10, 13]. These observations led to the hypothesis that an alternative phagocytic process performed by "amateur" phagocytes present in the injury core may complement macrophages/microglia for myelin debris clearance, at least in the early stages. Indeed, a recent report shows that astrocytes act as amateur phagocytes to participate in myelin debris clearance in MS[14]. However, this cannot be the case for SCI because astrocytes are absent from the epicenter of injured spinal cords.

Microvessels are present in the injury core as early as 3 days post-injury and their density increases up to 540% of that of normal conditions during the chronic phase of SCI[15, 16]. Following acute injury, the newly formed microvessels arise by angiogenesis, or proliferation of microvascular endothelial cells (ECs). It is known that ECs could act as amateur phagocytes to engulf large particles such as bacteria[17], apoptotic cell bodies[18] and latex particles[19]. Given the early presence and great number of newly formed microvessels in the injury core, we

hypothesize that microvessels and the lining microvascular ECs serve as amateur phagocytes for myelin debris uptake.

In the current study, we established a previously unidentified role for microvessels and lining microvascular ECs in engulfing and degrading myelin debris after SCI and experimental autoimmune encephalomyelitis (EAE), a commonly used animal model of MS. We also discovered a novel pathway for myelin debris degradation through the autophagy-lysosome system. Importantly, we demonstrated for the first time that microvascular EC uptake of myelin debris exerts critical functions beyond myelin debris clearance. Engulfment and autophagic processing of myelin debris by ECs have sequential consequences in promoting chronic inflammation and pathological healing (angiogenesis and fibrotic scar formation) during the progression of demyelinating disorders.

Results

Microvessels in the demyelinating spinal cords contain myelin debris

Microvessels in the lesion epicenter are lost during the first two days after SCI, whereas ECs give rise to newly formed microvessels from 3 days after injury, restoring microvessel density to a normal level by 1 week after SCI[15, 16]. We first examined whether these newly formed microvessels could engulf myelin debris. The uninjured spinal microvessels contain very little detectable myelin basic protein (MBP) (**Fig. 1a,a'**). By contrast, myelin debris started to closely associate with newly formed microvessels in the lesion core as early as 3 days post SCI (**Fig. S1**), and became more apparent at 5 or 7 days after SCI (**Fig. 1b, S1**). The *x-z* and *y-z* view of myelin debris distribution relative to microvessels revealed that myelin debris was indeed engulfed by microvessels (**Fig. 1b',S1**). Myelin debris-containing microvessels were frequently observed in the injured region and were much less frequently seen in the uninjured spinal cords following SCI (**Fig. 1d,S1**). Furthermore, neutral lipids, the

myelin degradation products that are stained with ORO, can be detected in microvessels at the injured core at 14 days after SCI (**Fig. 1e,e'**).

We next investigated whether our observation extends to other demyelinating disorders such as EAE mouse model (**Fig. S2a**). The sagittal sections of EAE spinal cords demonstrated that the typical demyelinating lesions were concentrated in lumbar and thoracic cords (**Fig. S2b**). We observed the myelin debris-containing microvessels in T10-T12 demyelinating segments of spinal cords after 1 week of EAE induction (**Fig. 1c,c',d**). These *in vivo* data from SCI and EAE models indicate that microvessels engulf myelin debris after demyelination.

In vitro BMECs-induced microvessel-like structures engulf myelin debris

Primary mouse brain microvascular endothelial cells (BMECs) grown on Matrigel could form microvessel-like structures[20]. After incubation with microvessel-like tubules, myelin debris was seen as scattered puncta around or within the tubules (**Fig. 1f**). A closer inspection of the distribution of myelin debris revealed the apparent dynamics of myelin debris entry (**Fig. 1f'**). Some myelin fragments appeared to be close to but were not in direct contact with the capillary surface, as indicated by a lack of co-localization with endothelial marker CD31 (**Fig. 1f'**). Other myelin fragments were in the process of entering, whereas still others had completely transited the luminal membrane, showing partial or full co-localization with CD31 (**Fig. 1f'**). These data confirm that myelin debris could be internalized by microvessels.

In vitro engulfment of myelin debris by BMECs

We next investigated the kinetics and mechanisms of microvascular engulfment of myelin debris by using primary BMECs and a BMEC cell line, bEnd.3. Both primary BMECs and bEnd.3 cells engulfed myelin debris in a time-dependent manner with predominant perinuclear distribution (**Fig. 2a,d**). After incubation with myelin debris, the number of myelin-laden ECs (myelin-ECs) and intracellular MBP were quantified by flow cytometry (**Fig. 2b**)

and ELISA (**Fig. 2c**), respectively. The kinetics of myelin engulfment by bEnd.3 cells exhibited inefficient engulfment from 24-48 hr, efficient engulfment from 48-72 hr, and saturated engulfment from 72-96 hr (**Fig. 2e,f**). EC uptake myelin debris was much slower than BMDMϕ, which showed rapid myelin engulfment as early as 1-3 hr (**Fig. S3**).

IgG opsonization is required for effective myelin debris engulfment by BMECs

Complement-3 receptor (CR3) and Mac-2 (Glactin-3) have been proposed as receptors for myelin debris phagocytosis by macrophages[21] (**Fig. S4a**). Blockage of CR3 or Mac-2 alone by neutralizing antibodies, or a combined blockage of CR3 and Mac2 did not affect myelin debris engulfment by BMECs (**Fig. 2g,S4b**,). Low-density lipoprotein receptor-related protein 1 (LRP1), a proposed receptor for MBP[22], was shown to mediate myelin debris phagocytosis by microglia, astrocytes and oligodendrocytes[14, 22]. However, BMEC engulfment of MBP-deficient myelin debris isolated from shiverer mice was not impaired (**Fig. S5**). These data suggest that CR3, Mac-2 or LRP1 have little role in mediating myelin debris uptake by ECs.

Macrophage phagocytosis is mediated by serum-derived opsonins including antibodies and complement proteins[23]. To evaluate the role of opsonins on myelin debris engulfment, we cultured BMECs with myelin debris in different concentrations of serum. BMEC engulfment of myelin debris was stronger in the presence of 5% serum than that in 1% serum (**Fig. S6**), and was significantly reduced or even abolished after withdrawal of serum from interaction medium for phagocytosis (**Fig. S6**), suggesting that the factor(s) in serum are required for BMEC engulfment of myelin debris. Heat-inactivation of complement in serum at 56℃ failed to prevent myelin uptake by BMECs, while serum IgG inactivation at 70℃[24, 25] significantly abrogated myelin debris engulfment (**Fig. 2h,i**), indicating serum IgG is required for myelin engulfment by BMECs. Supplement of IgG alone in serum-free medium or in IgG-inactivated serum rescued BMEC engulfment of myelin debris (**Fig. 2i**). Importantly, pre-coating myelin debris with IgG was sufficient for myelin engulfment by BMECs in the serum-free culture or IgG-

inactivated serum culture (**Fig. 2h,i**). These data indicate that IgG opsonization of myelin debris is necessary and sufficient for myelin engulfment by ECs.

Transcriptional profiles of ECs after engulfing myelin debris

To understand the cellular and molecular alterations in ECs after myelin debris uptake, we performed RNA sequencing of ECs with (myelin-ECs) or without myelin debris engulfment (naïve-ECs). Over 2,500 genes were significantly upregulated and over 4,000 genes were downregulated in myelin-ECs compared to naïve-ECs **(**Supplementary RNA sequencing Dataset, **Fig. 3a)**. The differentially expressed genes in myelin-ECs were enriched in a variety of processes or signaling pathways, mainly including metabolism, extracellular matrix formation, vesicle transport, inflammation and cell junctions among others **(Supplementary Table 1, Fig. 3b,c)**.

Noteworthy, among the top 50 upregulated genes in myelin-ECs, collagen genes including *Col1α2, Col5 α2, Col16α1, Col6α2*, all of which were remarkably upregulated **(Fig. 3b)** and confirmed by q-PCR **(Fig. 3d)**. The inflammatory genes including interleukin (IL)-related genes (*Il1rl1, Il4, Il5, Il13ra1)* and chemokine genes [*Ccl2 (also known Mcp-1) and Cxcl1*] were also upregulated in myelin-ECs **(Fig. 3b)**. q-PCR analysis confirmed the increased gene expression of *Il-4, Il-6, Mcp-1* and *iNOS* in myelin-ECs **(Fig. 3e)**. Myelin debris uptake also upregulated vesicles-encoding genes for lysosomes, autophagosomes and endosomes **(Fig. 3b)**. The downregulated genes in myelin-ECs are involved in Notch signaling pathway and cell adhesion/junction **(Fig. 3c)**, which is related to endothelial angiogenesis and permeability, respectively.

Engulfed myelin debris is delivered to lysosomal degradation system through autophagy pathway

We next examined subcellular localization of engulfed myelin debris. Myelin debris was predominantly delivered to lysosomes as revealed by co-localization between the majority of myelin particles and puncta positive for Lysotracker red (**Fig. 4a,a'**). Myelin debris uptake increased the size of the lysosomes, especially those containing

myelin debris (**Fig. 4a',b**). Lysosomes in naïve-ECs were 0.60 ± 0.02 μm in diameter (**Fig. 4a',b**). However, lysosomes that contained myelin debris (arrow) were 1.35 ± 0.03 μm, while lysosomes containing no myelin debris (arrowhead) in myelin-ECs were maintained around 0.64 ± 0.01 μm (**Fig. 4a',b**).

Cargo can be delivered through endocytosis or autophagy pathway to lysosomes for degradation[26]. We first examined whether myelin debris co-localizes with endosomes in BMECs. There was almost no or little co-localization between myelin debris and the early (Rab5)/late (Rab7) endosomes **(Fig. 4c,d)**, suggesting that endosomal machinery is not the primary route for myelin delivery to lysosomes.

RNA sequencing data revealed upregulation of autophagy genes including *Gabarapl2, Gabarap, Atg12, LC3b, Atg5* and *Atg3* in myelin-ECs (**Fig, 3b**). We next explored the possible role of the autophagy in delivering myelin debris to lysosomes. Myelin-ECs increased autophagosome formation (LC3b-puncta) significantly, while fed BMECs showed very few LC3b-puncta (negative control), and starvation induced robust formation of LC3b-puncta (positive control) **(Fig. 4e)**. A closer look at the relative localization between myelin debris and LC3-puncta revealed that majority of myelin debris was in contact with autophagosomes **(Fig. 4c,d)**. Myelin debris also showed significant co-localization with puncta positive for another autophagy marker GABARAP **(Fig. 4c,d)**. The western blot analysis demonstrated that myelin debris uptake induced LC3-I conversion to LC3-II **(Fig. 4f,S13)**, an indicator of autophagosomes formation. Moreover, myelin debris uptake caused autophagy substrate p62 degradation **(Fig. 4f),** indicating autophagy induction by myelin debris.

We next examined whether inhibiting autophagy-lysosome pathway could block myelin degradation in *Atg5* knockout (*atg5*$^{-/-}$) BMECs generated by CRISPR-Cas9 technique (**Fig. 4g,S7a,b,S13**). The *atg5*$^{-/-}$ BMECs maintained normal cell viability (**Fig. S7d**). The *atg5*$^{-/-}$ BMECs failed to generate LC3^{+} puncta (**Fig. 4h**) and induced LC3 conversion (**Fig. 4i, S13**), as well as accumulated p62 and ubiquitin (**Fig. 4i,S7c**), verifying the knockout is functional. *Atg5*$^{-/-}$ BMECs failed to degrade the engulfed myelin debris into neutral lipids (**Fig. 4j,k**). Consistently, either blocking autophagy using 3-MA, an inhibitor of autophagosome formation, or inhibition of lysosomal activity with chloroquine, significantly inhibited myelin degradation into neutral lipids in myelin-ECs

without causing apparent cell toxicity **(Fig. 4j,k,S7d)**. Conversely, additional supply of autophagosomes to myelin-ECs accelerated myelin degradation by rapamycin or starvation treatment (**Fig. 4j,k**). These genetic or pharmacological data indicate that autophagy-lysosome pathway is required for engulfed myelin debris degradation.

Microvessels are enlarged in SCI and EAE models

Although the microvessel density is remarkably increased during the subacute phase of SCI[15, 16], little attention has been paid to the change in the morphology and structure of the newly formed microvessels. Compared to the microvessels with a mean diameter of 8.17 ± 0.41 μm in normal spinal cords, the microvessels in the injured core increased the mean diameter to 16.66 ± 0.51 μm after 1 week post SCI **(Fig. 5a,b,S8a)**. These dilated microvessels were not only seen in the injured core at 1, 4, 6, 8 and 10 weeks following SCI, but also seen in the marginal regions **(Fig. 5a,b)**. The dilated microvessels in the injury region were proliferative, as indicated by Ki-67, a marker for cell proliferation **(Fig. 5c,c')**. Interestingly, microvessels in demyelinated regions were also enlarged (**Fig. 5d,d'**) and proliferative in the spinal cords from EAE mice (**Fig. 5e**). These data indicate that enlarged microvessels are common in demyelinating diseases.

Engulfment and autophagic processing of myelin debris promote EC proliferation and angiogenesis

We next sought to identify whether lesion-related factors stimulate microvascular growth. Myelin debris uptake significantly increased the Ki-67$^+$ proliferative ECs **(Fig. 5f)**. Cell populations were increased after exposure to myelin debris in a time-dependent manner **(Fig. 5g)**. The proliferative capacity of myelin-ECs was further confirmed by an *in vivo* matrigel angiogenesis assay. Subcutaneous injection of matrigel plugs containing myelin-ECs stimulated extensive angiogenesis **(Fig. 5h)**. Similarly, myelin-ECs injected into normal spinal cord remained highly proliferative and appeared integrated within microvasculature (**Fig. S8b**). It is noteworthy that

either injection of myelin alone or injection of ECs (ECs were exposed to, but not able to engulf myelin debris in the presence of IgG-inactivated serum) failed to induce angiogenesis (**Fig. S8b**). Moreover, *in vitro* myelin-induced EC proliferation was abrogated after *Atg5* knockout (**Fig. 5i**), indicating that autophagic degradation of myelin debris is required for EC proliferation. These data indicate that myelin debris gains proangiogenic potential only after being engulfed and intracellularly processed in ECs. The proangiogenic potential of myelin-ECs could likely be attributed to the increased expression of vascular endothelial growth factor (VEGF) **(Fig. 5j),** as VEGF neutralization blocked myelin-induced EC proliferation (**Fig. 5k**).

EC engulfment of necrotic cells inhibits cell proliferation

We wondered whether the necrotic cells generated after SCI could also affect EC proliferation and angiogenesis. BMECs were able to engulf the necrotic neuronal cells (**Fig. S9a,b**), but less efficiently when compared to BMDMϕ (**Fig. S9c**). Unlike myelin uptake, necrotic cell engulfment significantly inhibited BMEC growth (**Fig. S9d**). We tested this specificity in two additional assays. Zymosan, or dead yeast was efficiently engulfed by BMDMϕ (**Fig. S9g**), but could not be engulfed by BMECs (**Fig. S9h**) and had no effect on EC proliferation (not shown). We next tested whether the reactive astrocytes, which form glia scar around SCI lesion and are spatially distant from microvessels in the injured core. We mimicked this indirect interaction in a transwell assay (**Fig. S10a,b**), and found that either resting or reactive astrocytes induced by LPS had no significant effects on BMEC proliferation (**Fig. S10c**).

Myelin debris uptake by ECs stimulates inflammatory responses

We next sought to examine whether myelin debris-primed ECs promote inflammation by inducing leukocyte infiltration. We previously demonstrated that the bone marrow-derived cells that infiltrated to the injured spinal cord are mainly BMDMϕ using GFP^+ bone marrow chimeric mice[10]. Normal spinal cords had little or no GFP^+

BMDMϕ infiltration. However, GFP^+ BMDMϕ infiltrated in the injured core and closely associated with newly formed microvessels following 3 days post SCI **(Fig. 6a,S11a)**. The number of microvessel-associated BMDMϕ increased from 3 days to 1 or 2 weeks post SCI **(Fig. 6a,S11a)**, correlating with formation of enlarged microvessels in the injury core. Similarly in 1-week EAE mice spinal cord, infiltrated Iba-1^+ macrophages closely associated with enlarged microvessels in demyelinating regions (**Fig. 6b**). This correlation suggests macrophage recruitment is dependent on the newly formed microvessels, which may serve as a portal to facilitate BMDMϕ entry. Supporting this, a closer look at the infiltrated BMDMϕ showed that some BMDMϕ were bordering the outer surface of microvessels or were just entering the spinal cord **(Fig. 6a')**, indicating that they were in the process of or had completed transmigration across microvascular endothelium towards spinal cord parenchyma.

We next determined whether myelin debris uptake activates ECs, a critical step for leukocytes infiltration. There were a greater number of BMDMϕ adhering to the myelin-EC monolayer than that to the naïve-ECs (**Fig. 6c,c'**), probably due to the increased expression of vascular cell adhesion molecule-1 (VCAM-1) in myelin-ECs (**Fig. 6d, S13**). ECs did not increase BMDMϕ adhesion when ECs were exposed to myelin debris without IgG opsonization (**Fig. 6c',S11c**), where myelin debris was exposed to ECs without being engulfed. ECs with myelin uptake but no intracellular degradation (*atg5*$^{-/-}$ EC uptake myelin debris) did not increase BMDMϕ adhesion either (**Fig. 6c',S11c**), indicating that only intracellularly processed myelin debris is able to activate ECs and induce BMDMϕ adhesion. Besides macrophage adhesion, conditioned media from myelin-ECs, but not from naïve-ECs, remarkably stimulated BMDMϕ chemotaxis (**Fig. 6e**), suggesting that endothelial-derived factors from myelin-ECs stimulate BMDMϕ migration. We found that myelin debris significantly increased endothelial secretion of MCP-1 (**Fig. 6f**), the major chemokine for macrophage recruitment[27]. Myelin-ECs also upregulated other pro-inflammatory mediators (**Fig. 3b,e**), which may together contribute to BMDMϕ infiltration. Furthermore, myelin-ECs activated BMDMϕ, as evidenced by upregulated IL-6 expression in BMDMϕ after being exposed to myelin-EC conditioned media (**Fig. 6g**). We then examined the inflammatory potential of myelin-ECs by injection of naïve-ECs or myelin-ECs into normal spinal cords. Myelin-EC injection increased the number of Iba-1^+

macrophages/microglia and activated astrocytes compared to naïve-ECs injection (**Fig. 6h,S11e,f**). It is noteworthy that either injection of myelin alone or ECs (ECs were exposed to but not able to engulf myelin debris in the presence of IgG-inactivated serum) failed to induce inflammation *in vivo* (**Fig. S11d,e,f**), confirming that myelin debris uptake by ECs, but not simple exposure, promotes pro-inflammatory responses. Furthermore, we showed that engulfment of necrotic neuronal cells had no significant change in *Mcp-1* gene expression (**Fig. S9e**), indicating the specificity of EC engulfment of myelin debris in promoting inflammation.

Enlarged microvessels and ECs contribute to fibrotic components production

A fibrotic scar forms and occupies the injury core, which is typically characterized by extensive deposition of collagen[28] and fibronectin[29]. However, little is known about the cellular origin of such fibrotic scar in the injury core. Given the highly upregulated collagen genes in myelin-ECs **(Fig. 3b,d)**, we therefore examined the spatiotemporal relationship between microvascular ECs and collagen/fibronectin in the injured spinal cords. A low level of collagen 1 (Col1) expression in the normal cord was detected with a close association with microvessels **(Fig. 7a)**. However, at 6 weeks after SCI, a dense Col1 was present at the injury core and its expression pattern intimately resembled that of enlarged microvessels **(Fig. 7b)**. There was almost no expression of fibronectin throughout the normal spinal cords (**Fig. 7d**). Some, but not all microvessels are closely associated with fibronectin expression at 6 weeks after SCI **(Fig. 7e)**. Similarly, a dense Col1 or fibronectin co-localized well with enlarged microvessels in the spinal cords from EAE mice (**Fig. 7c,f**). Our *in vivo* data from two demyelinating models support that microvascular ECs could be a novel source of fibrotic scar formation through endothelial production of collagen and fibronectin.

RNA sequencing identified the top upregulated genes implicated in fibrosis, including collagen genes *Col1α2*, *Col5 α2*, *Col16α1*, and *Col6α2* in myelin-ECs **(Fig. 3b)**, suggesting that myelin debris has the potential to stimulate ECs to produce fibrotic components. BMECs treated with myelin debris for 1 day did not significantly

increase expression of Col1 (data not shown) or fibronectin **(Fig. 7i, S13)**, however, prolonged treatment with myelin debris significantly increased expression of Col1 (**Fig. 7g,g'**) and fibronectin **(Fig. 7i)** to a level similar to that of transforming growth factor β1 (TGF-β1) treatment, a strong inducer of collagen or fibronectin production[30]. Myelin debris also increased Col1 expression in microvessel-like structures (**Fig. 7h**), supporting the notion that myelin debris stimulates microvascular production of pro-fibrotic proteins in lesion core.

Engulfment and autophagic processing of myelin debris by ECs induce endothelial-to-mesenchymal transition (endoMT)

Interestingly, treatment with myelin debris for 10 days reduced CD31 expression in some BMECs **(Fig. 7g)**, a phenotype resembling endothelial-to-mesenchymal transition (endoMT), which has been implicated in tissue fibrosis in various diseases[31]. Control BMECs exhibited the characteristic polygonal cobblestone-like morphology **(Fig. 8a,c)**, while after treatment with TGF-β1, a strong inducer of endoMT[31] and myelin debris for 10 days, BMECs elongated and exhibited the same spindle-like morphology as fibroblasts **(Fig. 8a,c)**, a morphological change indicating the induction of endoMT. Additionally, exposure to TGF-β1 or myelin debris, but not to necrotic cells, markedly downregulated CD31 expression and strongly induced the expression of endoMT marker α-smooth muscle actin (α-SMA) in BMECs (**Fig. 8b,d,e,f**,**S9f**), indicating the specificity of myelin uptake by ECs in endoMT induction. Moreover, engulfment of myelin debris upregulated TGF-β1 expression (**Fig. 8g**), and blockade of TGF signaling by a pan-TGF-β neutralizing antibody abrogated myelin-induced endoMT phenotypes (**Fig. 8a,c**,**b,d**). Autophagic processing of myelin debris was crucial for myelin-induced endoMT because *atg5*$^{-/-}$ BMECs failed to show morphological change (**Fig. 8a,c**) and α-SMA expression (**Fig. 8b,d**). Noteworthy, at 6 weeks after SCI and 15 days of EAE, microvessels co-localized with CD31 and α-SMA, indicating *in vivo* endoMT following demyelination (**Fig. 8h**). Our data showed that myelin debris stimulates endothelial-derived fibrotic components, probably via endoMT.

Discussion

While BMDMϕ and microglia are the major phagocytes to clear myelin debris generated after demyelination, our data demonstrated that microvascular ECs act as amateur phagocytes to engulf myelin debris. We revealed that myelin debris uptake and autophagic processing by microvascular ECs have more important functions. EC uptake and processing of myelin debris cause a series of sequential events associated with disease progression, including inflammation, angiogenesis, and fibrotic scar formation.

Most of our knowledge of myelin debris phagocytosis comes from studies on macrophages and microglia. Receptors such as CR3, Mac-2, and LRP-1 are involved in myelin debris phagocytosis by macrophages/microglia[21]. Our study showed that ECs do not employ these receptors for myelin debris uptake. The "naked" myelin debris is not recognized by ECs and only IgG-opsonized myelin debris can be engulfed effectively, suggesting IgG receptors (FcγRs) are involved in myelin debris engulfment by ECs. Compromised BBB leads to leakage of IgG in the injured area[32], which may be the source of IgG for oposinization. Given the fact that brain ECs and other antigen presenting cells are able to engulf myelin debris and present myelin antigens to lymphocytes[33], the specific antibodies may further opsonize myelin debris and facilitate its engulfment. Endogenous antibodies have been shown to promote the rapid clearance of myelin debris in mouse[34], but it is unknown which cell type(s) benefit from the opsonization by antibody for myelin debris uptake. We speculate that ECs are the major cell type that relies on antibody opsonization of myelin debris for myelin debris clearance.

Autophagy is a fundamental degradative pathway for degradation of intracellular proteins and organelles. Autophagy has recently emerged as an alternative mechanism for myelin debris clearance in Schwann cells[35, 36]. Using autophagy-deficient ECs, we show that autophagy is required for myelin debris degradation in ECs. Furthermore, autophagic processing of myelin debris is crucial for proangiogenic, pro-inflammatory, and pro-fibrotic responses. However, if either ECs contact myelin debris but do not internalize it, or internalize myelin debris without autophagic processing, it does not elicit those responses, indicating that myelin debris causes consequences only after being engulfed and intracellularly processed.

The major vascular change in the injury area is angiogenesis during chronic stages of SCI. The newly formed microvessels in both SCI and EAE models are structurally abnormal, appearing dilated and more disorganized. The mechanisms and biological outcomes for these vascular abnormalities are poorly understood after demyelination. We demonstrated that myelin debris is one critical lesion-related factor that causes excessive EC proliferation, which may contribute to microvessel dilation at injury sites. Interestingly, the dilated microvessels in the injured spinal cords lose pericyte coverage in early stage of SCI[37], a cellular constituent in the neurovascular unit that has been recently reported to constrict microvessels[38]. Therefore, an alternative explanation for the microvessel dilation could be that these newly formed microvessels have defects in pericytes maturation or/and coverage, which thus fail to constrict microvessels and lead to microvessel dilation.

One of the most important features of neuroinflammation is the leukocyte recruitment, which requires the EC activation through an increased expression of VCAM-1 and cytokines/chemokines[39]. Myelin debris engulfment activates ECs by increasing expression of VCAM-1 and a variety of cytokines/chemokines that could facilitate BMDMϕ recruitment to injury site. Myelin debris might also promote BMDMϕ influx to injury site by increasing microvascular permeability to leukocytes, as indicated by the downregulation of genes related to cell junctions in myelin-ECs.

The fibrotic scars in the central region of injury sites, characterized by the excessive accumulation of collagen and fibronectin, have been known to inhibit axon regeneration[40]. Fibroblasts, which are prominent in the injured epicenter, contribute to fibrotic scar formation by stimulating the production of collagen[28] and fibronectin[29]. However, little is known about the cellular origin of fibroblasts in contusive injured spinal cords[28, 29, 41]. Our study demonstrated that enlarged microvessels contribute to the significant deposition of fibrotic components in SCI and EAE models. Soderblom *et al* reported contribution of perivascular fibroblasts from larger-diameter microvessels (in our study, we referred to them as enlarged or dilated microvessels) to Col1α1 production and fibrotic scar formation using Col1α1-GFP transgene, which is consistent with our results[28]. The

exact cellular identity of perivascular fibroblasts is not very clear, given that different cell types can share the same cell makers and some cell types can have further sub-types.

The activated fibroblasts, or myofibroblasts, may arise from other sources including resident fibroblasts, perivascular pericytes, bone marrow-derived precursors and others[42]. ECs have greater plasticity and can acquire fibroblast-like properties by undergoing endoMT[31]. Our study demonstrated that ECs could become fibroblasts-like cells after myelin uptake via endoMT. This suggests microvascular ECs are an additional source of fibroblasts or fibroblasts-like cells for fibrotic scar formation at the SCI lesion core. Interestingly, it takes a few days for myelin debris to significantly increase expression of fibronectin, collagen, and α-SMA in microvascular ECs, coinciding with the delayed accumulation of perivascular fibroblasts at the injury core[43]. We further determined that myelin debris induces endoMT via TGF-β1. TGF signaling has been known as a master regulator of endoMT[31] and participates in the formation of fibrotic scars in the injury site[44, 45]. The TGF-β signaling is activated in several cell types within SCI lesion, including macrophages, astrocytes and ECs[40, 46]. Thus, we propose that TGF signaling-mediated endoMT in ECs may underlie the effects of TGF signaling on fibrotic scar formation in SCI lesions.

In conclusion, we reveal that microvessels and lining microvascular ECs act as amateur phagocytes to engulf myelin debris generated by CNS disorders associated with prominent demyelination. Mechanistically, we determined that IgG opsonization of myelin debris is required for efficient uptake by microvascular ECs. The engulfed myelin debris is then delivered through autophagy-lysosome pathway for intracellular degradation. Functionally, engulfment and autophagy-dependent processing of myelin debris by microvascular ECs contribute to three critical processes that are closely associated with CNS demyelinating disorders: robust angiogenesis that results in excessive and abnormal microvessels, chronic inflammation, and endothelial-mediated fibrosis (**Fig. S12)**. Therefore, it may be possible to reverse the effects of myelin-ECs by targeting these particular processes (e.g., myelin debris uptake, autophagy and endoMT).

Acknowledgments

We thank C. Badland for the artwork of Supplemental figure 13. We thank W. Lin and JY. Wang for assisting in some animal experiments. We thank D. Meckes for providing reagents. We thank R. Nowakowski and G. Hammel for editing the manuscript, and thank F. Lin for help with some statistics. This work was supported by a visiting student scholarship granted to T.Z. from China Scholarship Council, Hong Kong Health and Medical Research Fund (03142036) and the National Basic Research Program of China (2014CB502200) to W.W., National Institutes of Health (R01GM072611-4) and National Science Foundation (DMS-1662139) to J.F., National Science Foundation (DMS-0714589, DMS-1661727) to Y.R.

Author contributions

Y.R. and Y.Z conceived the study. Y.R., Y.Z., and T.Z. designed the experiments and analyzed the data. T.Z. and Y.Z. executed most of the experiments. L.S. performed flow cytometry, guided MBP ELISA, led the sample preparation for RNA-sequencing. S.R.B., H.S., and W.W. established mouse EAE model and provided EAE spinal cord samples. Y.J. and C.L. designed CRISPR-Cas9 knockout of Atg5. Y.L. performed spinal cord injection and some SCI. A.R. analyzed the RNA-sequencing data. X.W. provided the preliminary phenotype on in vivo microvessel angiogenesis after SCI. Z.C. provided some preliminary SCI tissues. Z.H. assisted in tissues collection and cryosectioning. N.Z. assisted in western blot assay and some quantifications. X.S., J.L., J.F., and W.W. analyzed some data. T.M. helped design some experiments, contributed discussion and edited on the manuscript and figures. J.L., J.F., C.L., W.W., and G.W. contributed to discussion. Y.Z., Y.R., and T.Z. wrote the manuscript.

Competing Interests

The authors declare no competing interests.

References

1. Ahuja, C.S.*, et al.* Traumatic spinal cord injury. *Nature reviews. Disease primers* **3**, 17018 (2017).

2. Schwab, M.E. & Bartholdi, D. Degeneration and regeneration of axons in the lesioned spinal cord. *Physiological reviews* **76**, 319-370 (1996).

3. Franklin, R.J. & Ffrench-Constant, C. Remyelination in the CNS: from biology to therapy. *Nature reviews. Neuroscience* **9**, 839-855 (2008).

4. Chen, M.S.*, et al.* Nogo-A is a myelin-associated neurite outgrowth inhibitor and an antigen for monoclonal antibody IN-1. *Nature* **403**, 434-439 (2000).

5. Filbin, M.T. Myelin-associated inhibitors of axonal regeneration in the adult mammalian CNS. *Nature reviews. Neuroscience* **4**, 703-713 (2003).

6. Kotter, M.R., Li, W.W., Zhao, C. & Franklin, R.J. Myelin impairs CNS remyelination by inhibiting oligodendrocyte precursor cell differentiation. *The Journal of neuroscience : the official journal of the Society for Neuroscience* **26**, 328-332 (2006).

7. Syed, Y.A.*, et al.* Antibody-mediated neutralization of myelin-associated EphrinB3 accelerates CNS remyelination. *Acta Neuropathol* **131**, 281-298 (2016).

8. Jeon, S.B., Yoon, H.J., Park, S.H., Kim, I.H. & Park, E.J. Sulfatide, a major lipid component of myelin sheath, activates inflammatory responses as an endogenous stimulator in brain-resident immune cells. *Journal of immunology* **181**, 8077-8087 (2008).

9. Sun, X.*, et al.* Myelin activates FAK/Akt/NF-kappaB pathways and provokes CR3-dependent inflammatory response in murine system. *PLoS One* **5**, e9380 (2010).

10. Wang, X.*, et al.* Macrophages in spinal cord injury: phenotypic and functional change from exposure to myelin debris. *Glia* **63**, 635-651 (2015).

11. Napoli, I. & Neumann, H. Protective effects of microglia in multiple sclerosis. *Experimental neurology* **225**, 24-28 (2010).

12. Neumann, H., Kotter, M.R. & Franklin, R.J. Debris clearance by microglia: an essential link between degeneration and regeneration. *Brain : a journal of neurology* **132**, 288-295 (2009).

13. Guo, L.*, et al.* Rescuing macrophage normal function in spinal cord injury with embryonic stem cell conditioned media. *Mol Brain* **9**, 48 (2016).

14. Ponath, G.*, et al.* Myelin phagocytosis by astrocytes after myelin damage promotes lesion pathology. *Brain : a journal of neurology* **140**, 399-413 (2017).

15. Ng, M.T., Stammers, A.T. & Kwon, B.K. Vascular disruption and the role of angiogenic proteins after spinal cord injury. *Transl Stroke Res* **2**, 474-491 (2011).

16. Whetstone, W.D., Hsu, J.Y., Eisenberg, M., Werb, Z. & Noble-Haeusslein, L.J. Blood-spinal cord barrier after spinal cord injury: relation to revascularization and wound healing. *Journal of neuroscience research* **74**, 227-239 (2003).

17. Rengarajan, M., Hayer, A. & Theriot, J.A. Endothelial Cells Use a Formin-Dependent Phagocytosis-Like Process to Internalize the Bacterium Listeria monocytogenes. *PLoS pathogens* **12**, e1005603 (2016).

18. Dini, L.*, et al.* Phagocytosis of apoptotic bodies by liver endothelial cells. *J Cell Sci* **108 (Pt 3)**, 967-973 (1995).

19. Steffan, A.M., Gendrault, J.L., McCuskey, R.S., McCuskey, P.A. & Kirn, A. Phagocytosis, an unrecognized property of murine endothelial liver cells. *Hepatology* **6**, 830-836 (1986).

20. Arnaoutova, I. & Kleinman, H.K. In vitro angiogenesis: endothelial cell tube formation on gelled basement membrane extract. *Nat Protoc* **5**, 628-635 (2010).

21. Smith, M.E. Phagocytic properties of microglia in vitro: implications for a role in multiple sclerosis and EAE. *Microscopy research and technique* **54**, 81-94 (2001).

22. Gaultier, A.*, et al.* Low-density lipoprotein receptor-related protein 1 is an essential receptor for myelin phagocytosis. *J Cell Sci* **122**, 1155-1162 (2009).

23. Hart, S.P., Smith, J.R. & Dransfield, I. Phagocytosis of opsonized apoptotic cells: roles for 'old-fashioned' receptors for antibody and complement. *Clinical and experimental immunology* **135**, 181-185 (2004).

24. Jones, F.S. The Effect of Heat on Antibodies. *The Journal of experimental medicine* **46**, 291-301 (1927).

25. Vermeer, A.W. & Norde, W. The thermal stability of immunoglobulin: unfolding and aggregation of a multi-domain protein. *Biophysical journal* **78**, 394-404 (2000).

26. Tooze, S.A., Abada, A. & Elazar, Z. Endocytosis and autophagy: exploitation or cooperation? *Cold Spring Harb Perspect Biol* **6**, a018358 (2014).

27. Deshmane, S.L., Kremlev, S., Amini, S. & Sawaya, B.E. Monocyte chemoattractant protein-1 (MCP-1): an overview. *Journal of interferon & cytokine research : the official journal of the International Society for Interferon and Cytokine Research* **29**, 313-326 (2009).

28. Soderblom, C.*, et al.* Perivascular fibroblasts form the fibrotic scar after contusive spinal cord injury. *The Journal of neuroscience : the official journal of the Society for Neuroscience* **33**, 13882-13887 (2013).

29. Zhu, Y., Soderblom, C., Trojanowsky, M., Lee, D.H. & Lee, J.K. Fibronectin Matrix Assembly after Spinal Cord Injury. *J Neurotrauma* **32**, 1158-1167 (2015).

30. Ignotz, R.A. & Massague, J. Transforming growth factor-beta stimulates the expression of fibronectin and collagen and their incorporation into the extracellular matrix. *The Journal of biological chemistry* **261**, 4337-4345 (1986).

31. Piera-Velazquez, S., Mendoza, F.A. & Jimenez, S.A. Endothelial to Mesenchymal Transition (EndoMT) in the Pathogenesis of Human Fibrotic Diseases. *Journal of clinical medicine* **5** (2016).

32. Winkler, E.A., Bell, R.D. & Zlokovic, B.V. Central nervous system pericytes in health and disease. *Nature neuroscience* **14**, 1398-1405 (2011).

33. Lopes Pinheiro, M.A.*, et al.* Internalization and presentation of myelin antigens by the brain endothelium guides antigen-specific T cell migration. *eLife* **5** (2016).

34. Vargas, M.E., Watanabe, J., Singh, S.J., Robinson, W.H. & Barres, B.A. Endogenous antibodies promote rapid myelin clearance and effective axon regeneration after nerve injury. *Proceedings of the National Academy of Sciences of the United States of America* **107**, 11993-11998 (2010).

35. Brosius Lutz, A.*, et al.* Schwann cells use TAM receptor-mediated phagocytosis in addition to autophagy to clear myelin in a mouse model of nerve injury. *Proceedings of the National Academy of Sciences of the United States of America* **114**, E8072-E8080 (2017).

36. Gomez-Sanchez, J.A.*, et al.* Schwann cell autophagy, myelinophagy, initiates myelin clearance from injured nerves. *The Journal of cell biology* **210**, 153-168 (2015).

37. Hellstrom, M.*, et al.* Lack of pericytes leads to endothelial hyperplasia and abnormal vascular morphogenesis. *The Journal of cell biology* **153**, 543-553 (2001).

38. Li, Y.*, et al.* Pericytes impair capillary blood flow and motor function after chronic spinal cord injury. *Nature medicine* **23**, 733-741 (2017).

39. Wu, F., Liu, L. & Zhou, H. Endothelial cell activation in central nervous system inflammation. *Journal of leukocyte biology* **101**, 1119-1132 (2017).

40. Kawano, H.*, et al.* Role of the lesion scar in the response to damage and repair of the central nervous system. *Cell and tissue research* **349**, 169-180 (2012).

41. Fernandez, E. & Pallini, R. Connective tissue scarring in experimental spinal cord lesions: significance of dural continuity and role of epidural tissues. *Acta neurochirurgica* **76**, 145-148 (1985).

42. Hinz, B.*, et al.* The myofibroblast: one function, multiple origins. *The American journal of pathology* **170**, 1807-1816 (2007).

43. Zhu, Y.*, et al.* Hematogenous macrophage depletion reduces the fibrotic scar and increases axonal growth after spinal cord injury. *Neurobiology of disease* **74**, 114-125 (2015).

44. Logan, A.*, et al.* Effects of transforming growth factor beta 1 on scar production in the injured central nervous system of the rat. *The European journal of neuroscience* **6**, 355-363 (1994).

45. Yoshioka, N.*, et al.* Small molecule inhibitor of type I transforming growth factor-beta receptor kinase ameliorates the inhibitory milieu in injured brain and promotes regeneration of nigrostriatal dopaminergic axons. *Journal of neuroscience research* **89**, 381-393 (2011).

46. Fee, D.B., *et al.* Traumatic brain injury increases TGF beta RII expression on endothelial cells. *Brain research* **1012**, 52-59 (2004).

Figure legends

Figure 1. Engulfment of myelin debris by spinal microvessels in SCI and EAE mouse models and endothelial cells-induced microvessels-like structures *in vitro*. (**a, b, c**) Internalization of myelin debris (MBP staining, green) by microvessels (CD31 staining, red) in normal spinal cords from uninjured mice (**a**) and spinal cords from injured mice at 1 week after SCI (**b**) or 1 week of EAE (**c**). The *x-y, x-z* and *y-z* views (**a', b', c'**) show myelin debris internalized by microvessels in SCI and EAE spinal cords. (**d**) Quantification of myelin-containing microvessels in normal, SCI and EAE spinal cords. Myelin uninjured and injured regions were classified in SCI and classification details are described in materials and methods. Data are shown as means ± s.e.m. n=4 in SCI, n=3 in EAE. 1-d SCI, p=0.779 (*ns,* not significant); 3-d SCI, p=0.0111 (*); 5-d SCI, p=0.0088 (**); 7-d SCI, p=0.0121 (*); 7-d EAE, p=0.0076 (**) by paired two-sided Student's t-test. (**e, e'**) Detection of neutral lipids (ORO, red) in spinal microvessels from mice after 2 weeks of SCI (**e, e'**). (**e'**) 3D reconstruction of microvessel (CD31, green) shows accumulation of ORO^+ lipids inside microvessels. Representative images of 3 independent mice. (**f, f'**) Distribution of CFSE-labeled myelin debris (green) in primary BMECs-assembled microvessels-like structures (CD31, red) on Matrigel that were incubated with myelin debris for 72 hr. The *x-y* and *y-z* views of one region of interest show myelin debris approaching to but not contacting microvessels-like structures (**f'-1**), or starting to touch (**f'-2**) or entering (**f'-3**) microvessels-like structures. Representative images of 2 independent staining experiments. Scale bar, 50μm (**a, b, c**), 20μm (**a', b', c**), 10μm (**e**), 50μm (**g**), 5 μm (**g'**).

Figure 2. ***In vitro*** **engulfment of myelin debris by brain microvascular endothelial cells (BMECs).** (**a**) Representative confocal images showing engulfment of CFSE-labeled myelin debris (green) by primary BMECs

(CD31, red) after exposure to myelin debris for the indicated time points. Scale bar, 20 μm. (**b**) Flow cytometry detection of the percentage of primary BMECs with or without CFSE-myelin debris treatment for 72 hr. Data are shown as means ± s.e.m. (n=3 independent cell cultures). p=0.00009022 (****) by unpaired two-sided Student's t-test. (**c**) ELISA detection of intracellular MBP in primary BMECs treated with or without myelin debris for 72 hr. Data are shown as means ± s.e.m. (n=3 independent cell cultures). p=0.0144 (*) by unpaired two-sided Student's t-test. (**d**) Representative confocal images showing engulfment of CFSE-myelin debris (green) by bEnd.3 cell line (CD31, red) after myelin debris treatment for the indicated time points. Scale bar, 20 μm. (**e**) FACS detection of the percentage of bEnd.3 cell line treated with or without myelin debris at the indicated time points. Data are shown as means ± s.e.m. (n=3 independent cell cultures). Unpaired Student's t-test. 24 hr *vs* 0 hr, p=0.00009022 (****); 48 hr *vs* 0 hr, p =0.0004 (***); 72 hr *vs* 0 hr, p=0.000008798 (****); 96 hr *vs* 0 hr, p=0.000004488 (****); 96 hr *vs* 72 hr, p=0.1308 (*ns*) by unpaired two-sided Student's t-test. (**f**) ELISA detection of intracellular MBP in bEnd.3 cell line treated with or without myelin debris at the indicated time points. Data are shown as means ± s.e.m. (n=3 independent cell cultures). 24 hr vs 0 hr, p=0.1939 (*ns*); 48 hr *vs* 0 hr, p =0.0173 (*); 72 hr *vs* 0 hr, p=0.0006 (***); 96 hr *vs* 0 hr, p=0.0008 (***); 96 hr *vs* 72 hr, p=0.1884 (*ns*) by unpaired two-sided Student's t-test. (**g**) Representative confocal images showing CFSE-myelin debris uptake by BMECs pretreated with control IgG, CR3 or Mac-2 neutralizing antibodies. Scale bar, 20 μm. (**h**) Representative images showing BMEC engulfment of CFSE-myelin debris in serum heated at 56 ℃ for 20 min (to inactivate C3, left) or at 70 ℃ for 20 min (to inactivate IgG, middle) and IgG-opsonized myelin debris in IgG inactivated serum (right). Scale bar, 20 μm. (**i**) Corresponding quantification was analyzed by ELISA detection of intracellular MBP in BMECs treated with myelin debris, IgG-opsonized myelin debris for 72 hr in the medium containing normal serum, C3-inactivated serum, no serum, IgG-inactivated serum or IgG-supplemented serum, respectively. Data are shown as means ± s.e.m. (n=3 independent cell cultures). p=0.0005 (***), p=0.0011 (**) were calculated in comparison to normal serum group by unpaired two-sided Student's t-test. Among no serum groups, IgG-opsonized myelin *vs* control, p=0.0001 ($^{\#\#\#\#}$); IgG supplementation *vs* control, p=0.00003129 ($^{\#\#\#\#}$). Among IgG

inactivated groups, IgG-opsonized myelin *vs* control, p=0.0013 ($^{\#\#}$); IgG supplementation *vs* control, p=0.0029 ($^{\#\#}$).

Figure 3. **Transcriptome comparison of naïve-BMECs and myelin-BMECs**. (**a**) Heatmap comparing naïve-BMECs and myelin-BMECs for the top 50 most changed genes as determined by pairwise comparisons using DESeq2. Two biological replicates were used for RNA-seq analysis. Each biological replicate had a corresponding technical replicate. (**b, c**) The upregulated and downregulated genes enriched in different groups in myelin-BMECs. Values show $\log_2$-fold changes. Adjusted *P* value are in Supplemental Table 1 and Supplementary RNA sequencing Dataset. *P* values were corrected using a Benjamini-Hocheberg adjustment method to control for false discovery rate. (**d, e**) Quantitative RT-PCR analysis of gene expression related to pro-fibrotic (**d**) and inflammatory responses (**e**) in naïve-BMECs and myelin-BMECs. The gene expression was normalized to *GAPDH* (**d**) and *β-actin* (**e**). Data are shown as means ± s.e.m. (n=3 biologically independent replicates). Collagen 1α2, p=0.0001 (***); Collagen 1α1, p=0.0015 (**); Collagen 5α2, p=0.0028 (**); MCP-1, p=0.0000002956 (****); IL-6, p=0.00007280 (****); IL-4, p=0.0003 (***); iNOS, p=0.00004785 (****) by unpaired two-sided Student's *t*-test.

Figure 4. **Engulfed myelin debris is delivered through autophagosomes to lysosomes for degradation to lipids in BMECs**. (**a, a'**) Lysosomes stained with Lysotracker Red dye (red) in BMECs treated with or without CFSE-myelin debris (green) for 72 hr. The zoomed images (**a'**) show the detailed size and spatial relationship of lysosomes and engulfed myelin debris in naïve-BMECs and myelin-BMECs. Arrowheads indicate lysosomes containing no myelin debris, arrows indicate lysosomes containing engulfed myelin debris. Scale bar, 10μm (**a**), 1μm (**a'**). (**b**) Quantification of the lysosome size in naïve BMECs and myelin-BMECs. Each dot indicates lysotracker red positive puncta. Data are shown as means ± s.e.m. (n=142 for native ECs, n= 174 for lysosomes

without myelin, n=240 for lysosomes with myelin). p=3.56e-29 (****) by unpaired Student's t-test. (**c**) Representative confocal images and 3D heatmap of co-localization between CFSE-myelin puncta (green) and $LC3^+$ or $GABARAP^+$ autophagosomes (red), between myelin puncta (green) and $Rab5^+$ early endosomes (red), or $Rab7^+$ late endosomes (red). Scale bar, 1μm. (**d**) Co-localization analysis between myelin debris and other vesicular puncta as indicated. Data are shown as means ± s.e.m. from at least 10 images in three biological replicates. p=0.00002715 (****) for LC3 *vs* Rab5, p=0.0004806 (***) for LC3 *vs* Rab7, p=0.00005009 (****) for GABARAP *vs* Rab5, p=0.000315 (***) for GABARAP *vs* Rab7 by unpaired two-sided Student's t-test. (**e**) Quantification of $LC3^+$ puncta per cell in BMECs cultured with 5% serum (fed), after starvation for 6 hr (starved), after treatment with myelin debris for 72 hr (myelin-ECs). Data are shown as means ± s.e.m. from at least 3 independent experiments (n=3 for fed group, n=4 for starved and myelin debris groups). Starved *vs* fed, p=0.009 (**); myelin debris *vs* fed, p=0.0029 (**) by unpaired two-sided Student's t-test. (**f**) Immunoblot and densitometry quantification for LC3 and p62 in BMECs treated with myelin debris for 0, 24 hr and 72 hr. Data are shown as means ± s.e.m. from 3 independent immunoblots. LC3-II/LC3-I, p=0.0334 (*); p62/GAPDH, p=0.0301 (*) by unpaired two-sided Student's t-test. Uncropped blots are in Supplementary figure 13. (**g**) Immunoblot for Atg5 in the indicated $Atg5^{-/-}$ BMEC lines generated by CRISPR-Cas9 technique. This initial western blot screening was performed once, yielding three lines (#4, 6, 8) that are negative for Atg5 protein expression. Uncropped blots are in Supplementary figure 13. (**h**) Immunostaining of wild-type BMECs and #4 $Atg5^{-/-}$ BMECs for anti-LC3 (green) in HBSS starvation-induced autophagy. CD31 (red) and Hoechst (blue) staining labels ECs and nuclei, respectively. This LC3 staining verification was performed twice. Scale bar, 20 μm. (**i**) Immunoblot for LC3-I/LC3-II conversion and p62 in #4 $Atg5^{-/-}$ BMECs. This verification was performed once after initial screening in (**g**). Uncropped blots are in supplementary figure 13. (**j**) Myelin degradation into neutral lipids (stained by ORO) in myelin-laden $Atg5^{-/-}$ BMECs and wild-type (WT) BMECs treated with 10 μM chloroquine (24 hr), 1 μM rapamycin (24 hr). Scale bar, 20 μm. (**k**) Quantification of ORO^+ lipids in (**j**) as well as in myelin-BMECs after 48 hr treatment with 1 mM 3-MA, 24 hr culture in 0% FBS medium (starvation). Data are shown as means ± s.e.m. from 3 independent experiments. $Atg5^{-/-}$, p=0.0075 (**); 3-MA, p=0.0073 (**); Chloroquine (Chloro),

p=0.006 (**); Rapamycin (Rapa), p=0.0005 (***); starved, p=0.0178 (*) were calculated in comparison to WT by unpaired two-sided Student's t-test.

Figure 5. **Myelin debris uptake contributes to angiogenesis in SCI and EAE.** (**a**) Microvessels (CD31, red) in three different regions, classified as uninjured, marginal and injured regions (see methods for detailed classification) in an injured spinal cord from 1-week SCI mouse. Scale bar, 500 μm; 50 μm in zoomed images. (**b'**) Corresponding quantification of microvessel diameter in the normal spinal cord, uninjured region, marginal regions and injured regions from mice at 1-, 4-, 6-, 8- and 10-week after SCI. Data are shown as means ± s.d. The number of mice analyzed is: normal (n=5); 1-week (n=5); 4-week (n=4); 6-week (n=4); 8-week (n=4); 10-week (n=3). (**c**) Immunostaining for Ki-67 (green) and CD31 (red) in normal spinal cord from uninjured mice and injured spinal cord from 7 day SCI mice. The zoomed images showed the Ki-67$^+$ microvessels. Arrowheads indicate Ki-67$^+$ ECs. Scale bar, 50μm (upper images), 10μm (lower images). (**c'**) Corresponding quantification of Ki-67$^+$ ECs in normal spinal cords from uninjured mice and injured spinal cords from SCI mice. Data are shown as means ± s.e.m. Normal mice (n=4) and SCI mice (n=5). p=0.0029 (**) by unpaired two-sided Student's t-test. (**d**) Microvessels (CD31, red) and myelin (MBP, green) staining in 15-day EAE spinal cord. Arrowheads indicate enlarged microvessels in demyelinated regions (MBP negative). Scale bar, 50μm. 20μm in zoomed images to the right. (**d'**) Quantification of the microvessel diameter in non-demyelinated and demyelinated regions from 7-day and 15-day EAE spinal cords. Data are shown as means ± s.e.m. from 3 mice. 7-day, p=0.0107 (*); 15-day, p=0.0139 (*) by paired two-sided Student's t-test. (**e**) Immunostaining for Ki-67 (green) and CD31 (red) in spinal cord from 15 day EAE mouse. Arrowheads indicate Ki-67$^+$ ECs on microvessels. Scale bar, 20μm. (**f**) Quantification of Ki-67$^+$ cells in primary BMECs and bEnd.3. cell line treated with myelin debris for 72 hr or the indicated time points. Data are shown as means ± s.e.m. naïve ECs (n=4 independent cultures), myelin-ECs (n=3 independent cultures). Primary BMECs, p=0.026 (*). bEnd.3. cell line, 72 hr, p=0.0226 (*); 96 hr, p=0.0118 (*); 120 hr, p=0.001 (***) by unpaired two-sided Student's t-test. (**g**) Number of BMECs treated with myelin debris

for the indicated time points. Data are shown as means ± s.e.m. from 3 independent assays. 72 hr, p=0.0026 (**), 96 hr, p=0.00001087 (****); 120 hr, p=0.0079 (**) by unpaired two-sided Student's t-test. (**h**) Gross images of Matrigel plugs injected subcutaneously with PBS, naïve ECs and myelin-ECs in normal mice. Insets are CD31 immunostaining of Matrigel slices. Scale bar in insets, 20μm. The bottom showed the corresponding quantification of $CD31^+$ microvessels in each Matrigel plug. Data are shown as means ± s.e.m. from 3 independent Matrigel plugs. Myelin-ECs *vs* naïve ECs, p=0.0002 (***) by unpaired two-sided Student's t-test. (**i**) Cell number of wild-type or $Atg5^{-/-}$BMECs with or without myelin debris treatment for 72 hr. Data are shown as means ± s.e.m. from 3 assays. p=0.0401 (*) by unpaired two-sided Student's t-test. (**j**) qRT-PCR analysis of VEGF expression in naive BMECs and myelin-ECs. Gene expression was normalized to *GAPDH*. Data are shown as means ± s.e.m. from 3 biologically independent replicates. p=0.0000000681 (****) by unpaired two-sided Student's t-test. (**k**) Cell number of BMECs treated with myelin debris in the presence of control IgG or neutralizing VEGF antibody (20 μg/ml, 72 hr). Data are shown as means ± s.e.m. (n=3 independent cultures). p=0.61 (*ns*), p=0.0184 (*) by unpaired two-sided Student's t-test.

Figure 6. **Myelin debris uptake induces endothelial inflammation leading to BMDMϕ infiltration.** (**a, a'**) Representative confocal images (**a**) and 3-D reconstructed images (**a'**) showing the spatiotemporal distribution of bone marrow-derived GFP^+ cells (GFP^+ BMDCs) and $CD31^+$ microvessels (red) in normal and injured spinal cords from GFP^+ bone marrow chimeric mice at 3 days, 1 week and 2 weeks after SCI. Scale bar, 20μm. Quantification data is shown in Supplemental figure 12a. (**b**) Representative confocal images and 3-D reconstructed images showing the spatial distribution of Iba-1^+ cells relative to microvessels (red) in 1-week EAE spinal cord. Scale bar, 20μm. Quantification data is shown in supplemental figure 12b. (**c**) Representative images showing adhered BMDMϕ (Mac-2, red) on the monolayer of naïve-ECs or myelin-ECs (DIC imaging, grey). Scale bar, 100μm. (**c'**) Corresponding quantification of adhered BMDMϕ on BMECs in (**c**) and $Atg5^{-/-}$ BMECs as well as WT BMECs cultured with 70°C heated serum (that is, no IgG or IgG-inactivated serum), the value was

shown as the percentage of adhered BMDMϕ relative to the underlying BMECs. Data were presented as means ± s.e.m. (n=3 independent cultures). p=0.0023 (**); p=0.0072 ($^{\#\#}$); p=0.0129 ($^{\#}$) by unpaired two-sided Student's t-test. (**d**) Immunoblot and quantification of VCAM-1 expression in BMECs treated with myelin debris for the indicated time points. Quantification of VCAM-1 expression level was determined by densitometry analysis relative to GAPDH. Data were presented as means ± s.e.m. (n=3 independent immunoblots). 1d, p=0.024 (*); 2d, p=0.0008 (***); 3d, p=0.0013 (**); 4d, p=0.0011 (**); 5d, p=0.0012 (**) by unpaired two-sided Student's t-test. Uncropped blots are in Supplementary figure 13. (**e**) Images of migrated BMDMϕ (violet crystal staining) towards conditioned media from ECs. BMDMϕ were added to the upper chamber and allowed to migrate through the membrane into the lower chamber containing conditioned media from naïve-ECs or myelin-ECs. This assay was performed twice with similar results. (**f**) ELISA detection for chemokine MCP-1 secreted by naïve-ECs or myelin-ECs in primary EC cultures (left) or cell line (right). Data were showed as means ± s.e.m. n=3 independent cell cultures. p=0.0006 (***), p=0.0029 (**) by unpaired two-sided Student's t-test. (**g**) Quantitative RT-PCR analysis of IL-6 in BMDMϕ treated with conditioned media from naïve-ECs or myelin-ECs. Gene expression was normalized to *β-actin*. Data were presented as means ± s.e.m. (n=3 biologically independent replicates). p=0.0002 (***) by unpaired two-sided Student's t-test. (**h**) Immunostaining of macrophages/microglia (Iba-1, green) and astrocytes (GFAP, red) in normal spinal cords injected with CFSE-labeled naïve ECs or myelin-ECs (white). Quantification data is shown in Supplemental figure 11e and 11f. Scale bar, 100 μm, 10 μm (inset images).

Figure 7. **Myelin debris engulfment promotes endothelial deposition of pro-fibrotic components.** (**a, b, c**) Immunostaining for collagen I (green) and CD31 (red) in normal spinal cords (**a**) and in the lesion cores from mice at 6 weeks after SCI (**b**) and in 15-day EAE spinal cord (**c**). Scale bar, 500 μm (upper images), 20 μm (lower zoomed images). Representative images of 3 independent mice. (**d, e, f**) Immunostaining for fibronectin (green) and CD31 (red) in normal spinal cords (**d**) and in the lesion cores from mice at 6 weeks after SCI (**e**) and in 15-day EAE spinal cord (**f**). Scale bar, 500 μm (upper images), 20 μm (lower zoomed images). Representative images

of 3 independent mice. (**g**) Immunostaining of collagen I (green) and CD31 (red) in BMECs treated with or without CFSE-myelin debris (pseudo white) for 10 days or treatment with moue recombinant TGF-β1 (10 ng/ml) for 3 days. Scale bar, 20 μm. (**g'**) Quantification of fluorescent intensity of collagen I in (**g**), Data are shown as means ± s.e.m. (n=3). Myelin *vs* control, p=0.0301 (*); TGF-β1 *vs* control, p=0.0159 (*) by two-sided Student's *t*-test. (**h**) Immunostaining of collagen I (green) in BMEC-induced microvessels-like structures (CD31, red) treated with or without CFSE-myelin debris (pseudo white) for 72 hr. Scale bar, 100 μm. This staining was performed twice with similar results. (**i**) Immunoblot for fibronectin in BMECs at baseline or after treatment with myelin debris for the indicated time points. Treatment with TGF-β1 (10 ng/ml) for 5 days was used as positive control. Corresponding quantification of protein levels was determined by densitometry analysis relative to GAPDH or tubulin, as shown at the bottom of each blot. The immunoblots were performed twice with similar results. Uncropped blot is in Supplementary figure 13.

Figure 8. Myelin debris engulfment induces endothelial-to-mesenchymal transition (endoMT).

(**a**) Phase contrast images of WT and $Atg5^{-/-}$ BMECs with the indicated treatment: TGF-β1 (10 ng/ml, 3 days), myelin debris (1mg/ml, 10 days), myelin + pan-TGF-β neutralizing antibody (20μg/ml, 10 days). The insets showed the magnified views of cell morphology. Scale bar, 100 μm. (**b**) Immunostaining of α-SMA (green) and CD31 (red) of WT and $Atg5^{-/-}$ BMECs with the indicated treatment as above, myelin debris is shown in pseudo white. The zoomed images below showed the detailed immunostainings of α-SMA, CD31 and engulfed myelin debris. Scale bar, 20 μm (upper images), 10 μm (lower images). (**c**) Quantification of spindle-shaped BMECs. The left diagram showed the criteria for spindle-shape cells. Data are shown as means ± s.e.m. (n=3 independent assays). p=0.0008 (***), p=0.0027 (**) *vs* control, p=0.0029 ($^{\#\#}$), p=0.001 ($^{\#\#\#}$) *vs* WT myelin group, analysis by unpaired two-sided Student's *t*-test. (**d**) Quantification of $\alpha\text{-SMA}^{+}$ $CD31^{+}$ BMECs. Data are shown as means ± s.e.m. (n=3 independent assays). TGF-β1 *vs* control, p=0.0015 (**); myelin *vs* control, p=0.0063 (**); myelin + TGF-β Ab *vs* myelin, p=0.0094 ($^{\#\#}$); myelin + $Atg5^{-/-}$ *vs* myelin + Wild-type, p=0.0063 ($^{\#\#}$), analysis by unpaired

two-sided Student's *t*-test. (**e**) Quantitative RT-PCR analysis of α-SMA expression in naïve ECs and myelin-ECs. Gene expression was normalized to *GAPDH*. Data are shown as means ± s.e.m. from 3 biologically independent replicates. p=0.0057 (**) by unpaired two-sided Student's *t*-test. (**f**) Immunoblot for α-SMA in BMECs at baseline or treatment with myelin debris for the indicated time points. Treatment with TGF-β1 (10ng/ml) for 5 days was used as positive control. Corresponding quantification of protein levels were determined by densitometry analysis relative to GAPDH or tubulin, as shown at the bottom of each blot. The immunoblots were performed twice with similar results. Uncropped blot is in Supplementary figure 13. (**g**) Quantitative RT-PCR analysis of gene expression of TGF-β1 in naïve ECs and myelin-ECs. Data are shown as means ± s.e.m. from 3 biologically independent replicates. Gene expression was normalized to *β-actin*. p=0.0002 (***) by unpaired two-sided Student's *t*-test. (**h**) Immunostaining for α-SMA (green) and CD31 (red) in normal spinal cords and in the lesion cores from mice at 6 weeks after SCI and 15 days of EAE. The staining was performed in three mice with similar results. Scale bar, 20μm (images to the left), 5μm (zoomed images to the right).

Methods

Reagents

Chemical reagents were purchased from Sigma-Aldrich (St. Louis, MO) and cell culture media was purchased from Invitrogen (Carlsbad, CA), unless otherwise indicated. Carboxyfluorescein succinimidyl ester (CFSE; #C1157) was from Life Technologies (Carlsbad, CA). 3-Methuladenine (3-MA; BML-AP502) was from Enzo Life Sciences (Farmingdale, NY). Rapamycin (#553210) was purchased from EMD Millipore (Burlington, MA). Recombinant mouse TGF-β1 (#5231) was from Cell Signaling Technology (Danvers, MA). Mouse MCP-1 ELISA kit (#432701) was from Bio Legend (San Diego, CA). Matrigel matrix growth factor reduced (#354230) was from BD Biosciences (San Jose, CA). Lysotracker red DND-99 (L7528; 1:5,000 for staining) was purchased from Invitrogen.

Antibodies

Anti-CD31 (#550274; 1:100 for IF) was from BD Biosciences (Franklin Lakes, NJ). Anti-MBP (ab40390; 1:200 for IF; 1:1,000 for ELISA), anti-Ki-67 (ab15580; 1:200 for IF), anti-CD11b (ab133357; 1:100 for IF), anti-Von Willebrand Factor (vWF; ab11713; 1:100 for IF), anti-α-SMA (ab124964; 1:400 for IF), anti-fibronectin (ab23750; 1:200 for IF; 1:1,000 for WB), anti-collagen I (ab34710; 1:200 for IF), anti-GFAP (#ab53554, 1:400 and GAPDH (ab181602; 1:3,000 for WB) were purchased from Abcam (Cambridge, MA). The antibodies against LC3 (#4108; 1:100 for IF; WB 1:1,000), Atg5 (D5F5U, #12994, 1:1000 for WB), Rab5 (#3547; 1:50 for IF), Rab7 (#9367; 1:100 for IF) and GABARAP (#13733; 1:200 for IF) were purchased from Cell Signaling Technology (Danvers, MA). Another anti-MBP (MAB386; 1:1,000 for ELISA) was purchased from Millipore (Billerica, MA), anti-VCAM-1 (sc-8304; 1:250 for WB) was purchased from Santa Cruz Biotechnology (Dallas, TX) and anti-Lamp1 (1D4B; 1:25 for IF) was from Developmental Studies Hybridoma Bank. Anti-tubulin (DM1A; 1:5,000 for WB) was from Sigma-Aldrich (St. Louis, MO). Anti-p62 (PM045; 1:1,000 for WB) was from MBL (Woburn, MA). Anti-ubiquitin (FK2, #BML-PW8810-0500; 1:200 for IF) was from ENZO Life

Sciences. Anti-Iba-1 (#019-19741, 1:200 for IF) was from FUJIFILM Wako Pure Chemical Corporation (Osaka, Japan). F4/80 and Mac-2 antibodies were produced by hybridoma cell lines (HB-198 for F4/80; TIB-166 for Mac-2) from American Tissue Culture Collection (ATCC, Manassas, VA). VEGF neutralizing antibody (#AF-493-NA, 20μg/ml for neutralization) and pan-TGF-β neutralizing antibody (#MAB1835R-100, 20μg/ml for neutralization) were from R&D Systems (Minneapolis, MN). Alexa Fluor 488, 555, 647-conjuated secondary antibodies (1:600 for IF) and HRP-conjugated secondary antibody (1:3,000 for ELISA) were purchased from Invitrogen. IRDye-800CW or IRDye-680LT-conjugated secondary antibodies (1:20,000 for WB) were from LI-COR Bioscience.

Mice

C57BL/6J, C57BL/6-Tg (ACTB-EGFP)1Osb/J and C3Fe.SWV-MBP^{shi}/J mice were purchased from Jackson Laboratory (Bar Harbor, ME) and maintained in pathogen-free animal facility in Florida State University. All animal protocols were approved by the Animal Care and Use Committee (ACUC) of Florida State University, except that the EAE induction protocol was approved bythe Committee for Use of Live Animals in Teaching and Research at The University of Hong Kong. No statistical methods were used to pre-determine sample sizes and our sample size was chosen according to standard practices in the field. Litter mates were ear tagged and randomly assigned to different experimental groups. Experimenters were blinded to animal surgeries and scoring. Quantification of microvessel diameter was performed independently by two blinded experienced researchers.

Spinal cord injury in mice

Thoracic spinal cord contusion injuries were performed on 8-10 week old C57BL/6J female mice. To expose the spinal cord, a laminectomy was performed on the T10 vertebrae. The contusion injury was induced using the NYU impactor with a 5 gram rod dropped 6.25mm from the cord surface [47]. Mice in the sham group were subjected to only a laminectomy without a contusion.

Active EAE induction in mice

EAE induction was performed as described previously with minor modifications [48, 49]. All the animal experiments were approved by the Committee for Use of Live Animals in Teaching and Research at The University of Hong Kong. 7-8 week old female C57BL/6J mice were used for EAE induction. The animals were housed in the Laboratory Animal Unit on a 12hr day/night cycle, with food and water ad libitum, and were allowed to acclimatize for 1 week before disease induction.

Female mice were subcutaneously immunized with 200 μg MOG35–55 peptide (Genscript, Piscataway, NJ) in complete Freund's adjuvant (3 mg/ml). Freshly prepared pertussis toxin (PHZ1174, ThermoFisher, 250 ng) in sterile PBS was injected intraperitoneally on day 0 and 48 h later.

EAE symptoms were scored daily as follows: 0, no clinical signs; 0.5, partially limp tail; 1, paralyzed tail; 1.5, hindlimb paresis or loss in coordinated movement; 2, loss in coordinated movement and hindlimb paresis; 3, one hindlimb paralyzed; 4, both hindlimbs paralyzed; 5, hindlimbs paralyzed, weakness in forelimbs; 6, moribund.

Generation of GFP$^+$ bone marrow chimeras

GFP$^+$ bone marrow chimeric mice were generated according to previous publication [10]. Briefly, female C57BL/6 mice of 8–10 weeks of age were exposed to irradiation with 10 Gy X-ray and then intravenously injected with 5×10^6 bone marrow cells freshly collected from transgenic mice (C57BL/6-Tg(ACTB-EGFP)1Osb/J) constitutively expressing GFP. Efficient reconstitution was confirmed by postmortem examination of circulating blood for GFP$^+$ cells. On average, 80% the transplant engraftment efficiency was achieved.

Cell cultures

See Supplementary Methods for source and culture information on primary mouse brain microvascular endothelial cells, a cell line of BMECs (bEnd.3), a mouse neuroblastoma cell line (Neuro-2a) and bone marrow-derived macrophages (BMDMϕ).

Generation of Atg5 knockout EC cell line by CRISPR/Cas9 technique

Single guide RNA sequence, atgaaggcacacccctgaaa, was selected to target the third exon of mouse Atg5 gene. The expression of guide RNA & scaffold RNA is driven under U6 promoter. The U6 promotor and guide & scaffold cassette was incorporated into a Cas9 expressing backbone vector tagged with EGFP. The sequence of the U6 promotor, guide RNA & scaffold RNA were confirmed by the sequencing, then transfected into mouse endothelial cells line bEnd.3 using FuGENE® 6 (#E2693, Promega) followed by the FACS sorting process. The method for CRISPR-Cas9 has not been published and a full characterization of this method will be published elsewhere. 48 hr later, cells were trypsinized into single cells, and sorted according to the GFP^+ signal into 96-well plate. After colony expansion, the protein expression of Atg5 was analyzed by western blotting. The genomic DNA was extracted from those clones which completely lost the Atg5 protein expression, then the targeted region was PCR amplified with the primer set flanked the targeted region. PCR amplicons was purified with the PCR purification kit (#28104, QIAGEN), and T7E1 (#E3321, NEB) assay was carried out to confirm the mismatch occurred at very specific site.

Preparation and fluorescent labeling of myelin debris

Myelin debris was isolated as described previously [9]. See Supplementary Methods for detailed information.

Myelin debris uptake assay

CFSE-labeled myelin debris was added to the BMECs cultures for indicated time periods at a final concentration of 1mg/ml. Non-ingested myelin debris was washed away from cell surface with EDTA for 30 seconds, citric acid for 1 min. Myelin debris uptake was analyzed by standard assays including confocal fluorescent imaging, flow cytometry and ELISA detection of intracellular MBP as described below.

See Supplementary Methods for detailed information on the role of CR3 or Mac-2, serum concentration and IgG or complement opsonization in EC uptake of myelin debris.

Flow cytometry analysis of myelin debris uptake

BMECs were treated with or without CFSE-labeled myelin debris for 72 hr, and washed to remove non-ingested myelin debris. BMECs were collected and resuspended in PBS, followed by immediate detection with a BD FACS Canto flow cytometer (Becton Dickinson).

Enzyme-linked immunosorbent assay (ELISA) detection of engulfed myelin debris

To detect the engulfed myelin debris in ECs, we performed MBP-specific sandwich ELISA as previously described [13, 50], with rabbit MBP antibody being the capturing antibody and rat MBP antibody being the detecting antibody. See Supplementary Methods for detailed information.

Myelin debris engulfment by microvessels-like structures

Primary BMECs were seeded on the polymerized Matrigel and cultured at 37 ℃ for 24 hr to form the tubular structures and then incubated with CFSE-myelin debris. After removal of non-ingested myelin debris, cells on Matrigel-coated coverslips were fixed with 2% paraformaldehyde (PFA), followed by regular immunostaining. Images were acquired with Nikon A1 laser scanning confocal microscope (Nikon, Japan) and the slice view of the tubular structures from both *x-y* axis and *x-z* axis were collected from the Nikon Elements analysis software.

Histology and immunofluorescent staining

See Supplementary Methods for details.

Oil Red O (ORO) staining

ORO staining was performed to detect intracellular neutral lipid accumulation in injured spinal cords and cultured BMECs. Spinal frozen sections or fixed cells were dehydrated in 100% propylene glycol for 5 min, then stained with 0.5% ORO solution at 60°C for 8 min. The samples were then processed with 85% propylene glycol for 5 min followed by distilled water rinsing for 3 times. Stained samples were imaged with a confocal laser scanning microscope.

Histology quantification

Quantifications of microvessel size were performed by unbiased researchers. To quantify the size of microvessels in three consecutive regions (injured, marginal and uninjured) of SCI, we first classified the three regions with GFAP staining as a major reference according to a previous publication with modification [51]. Using Nikon NIS-Elements software, the total area of the spinal cord and the area of the $GFAP^+$ regions were outlined and measured at 200μm intervals over a 2 mm distance, centered on the lesion core. The injured regions were defined as the regions spanning with a radius of around 300 μm, which were negative for GFAP but densely positive for nuclear staining (Hoechst staining). The marginal regions, within the $GFAP^+$ glia scar, were considered as 300-600 μm away from the epicenter, and the uninjured regions were considered as regions >600 μm away from the epicenter. We usually analyzed the normal regions that were more than 1000 μm away from epicenter. For microvessel size quantification in mouse EAE spinal cords, we measured microvessel diameter in both non-demyelinated and demyelinated regions in T10 segment. At least 20 microvessels with clear CD31 signals on each region were included for diameter analysis using image J Pro Plus 6.0 (Media Cybernetics, Rockville, MD).

To quantify the microvessel uptake of MBP^+ myelin debris in mouse SCI samples, we focused on uninjured and injured regions as classified above. The uninjured region represents the region without myelin debris and the injured region represents the region that accumulates myelin debris. The microvessel uptake of MBP^+ myelin debris in mouse EAE samples was quantified in T10 regions at early time points (pre-onset stage). X-Y, X-Z and Y-Z views were included to carefully assess the presence of myelin puncta within microvessels. Microvessels containing at least one fluorescently clear MBP^+ puncta were considered as myelin-containing microvessels.

To quantify the Ki67 positive microvessels in SCI samples, the microvessels positive for both Ki67 and CD31 staining were counted in the injured regions of 1-weeks post SCI or normal spinal cords.

For quantification of GFP^+ BMDC infiltration across microvessels at different time points of SCI, we stained spinal cord tissues with CD31 in GFP^+ bone marrow chimeric mice after SCI and counted the number of GFP^+ BMDCs that are closely associated with microvessels in one whole field with an area of 0.044 mm^2.

For quantification of Iba-1$^+$ cells in EAE microvessels, we stained Iba-1 and CD31 in T10 segment of 7 and 15 days post EAE spinal cords and counted the number of Iba-1$^+$ cells showing close association with per normal-sized or enlarged microvessels.

Autophagy assays, measurements and co-localization analysis

See Supplementary Methods for autophagy markers LC3 or GABARAP staining and analysis.

Lysotracker red staining and analysis

See Supplementary Methods for details.

Starvation and drug treatments for autophagy assays

See Supplementary Methods for details.

Propidium iodide (PI) staining assay for cell death analysis

The fixed BMECs were stained with PI and Hoechst, followed by imaging and quantification of PI positive nucleus using Nikon Element software. See Supplementary Methods for more information.

Image acquisition

Samples from spinal cords and cell culture were imaged with a Nikon Ti-E microscope (Nikon Instruments, Melville, NY) using 10×objective for large images acquisition with 25% overlapping. Regions of interest were imaged with Nikon A1 laser scanning confocal microscope using a 20×objective or a 60×/1.49NA oil immersion objective. All confocal images were acquired with a spacing of 0.25 μm or 0.5 μm between *z*-sections in Nikon NIS-Elements software and are maximum intensity projections of *z* stacks. In some images, volume view of *xyz* axis with or without 3D rendering, and slice view of *x-y, x-z* or *y-z* axis were applied. Gamma correction was applied in some images.

RNA-sequencing and data analysis

Mouse brain microvascular endothelial cells (bEnd.3) were plated at equal density in cell culture dishes and allowed to rest overnight prior to the addition of 1mg/mL myelin debris prepared as previously described. Total RNA was isolated from each of 2 biological replicates for control and myelin debris treated cells for 72 hours using the TRIzol® Plus RNA Purification Kit (Thermo Fisher). Selection of mRNA from total RNA was accomplished using the NEBNext Poly(A) mRNA Magnetic Isolation Module (NEB #E7490). From the total mRNA obtained, cDNA was generated using the high fidelity ProtoScript II Reverse Transcriptase (NEB) with a random primer mix to generate fragments. The double-stranded cDNA was purified using 1.8X Agencourt AMPure XP Beads prior to end preparation for adaptor ligation. The ligation reaction was performed using AMPure XP Beads and enriched via PCR and followed by a final purification using the Agencourt AMPure XP Beads. Quality of the resulting library was examined using Agilent High Sensitivity DNA Bioanalyzer Chips (Agilent Technologies 5067-4626) and quantified by KAPA Library Quantification Kits for Illumina sequencing platforms (KAPA Biosystems KK4824). Single-end sequencing was performed on the Illumina HiSeq 2000 DNA Sequencer in the Florida State University Department of Biomedical Sciences Translational Sciences Facility.

For mRNA-seq data analysis, the resulting sequences were trimmed of their Illumina indexing adaptors using Trimmomatic [52]. All reads between 50 and 100 bases were included in further analyses. Any reads with greater than 2 Ns were considered to be low quality, and thus discarded. Unique reads were aligned to the *Mus musculus* genome using TopHat2. A total of 4 mismatches between the reference genome and sample were allowed during alignment to account for strain differences between the endothelial cell line and the C57BL/6 reference genome. The TopHat2 mapped reads were further processed (filtered, sorted and indexed) with Samtools such that reads mapped to a single gene were used for further analysis [53, 54]. The uniquely mapped reads were then used to generate counts for each annotated gene using HTSeq (from Bioconductor version 3.0.2) [55]. Finally, differential expression analysis of count tables for control versus myelin debris treated comparisons at each time point was performed in DESeq2 (1.8.1, Benjamini-Hochberg FDR correction) [56-58].

Quantitative RT-PCR

Total RNA from cells was extracted using TRIzol. cDNA was reverse transcribed from 1μg of RNA using qScript Flex cDNA Synthesis Kit (#95047; Quanta Biosciences, Beverly, MA) according to the manufacturer's instructions. A total of 20 μL reaction system was prepared for quantitative RT-PCR using perfecta SYBR Green supermix (#95054; Quanta Biosciences). All reactions were run in triplicates using a real-time PCR system (CFX96; BioRad), and the specificity of every reaction was determined by a melting curve analysis. The expression level of target genes was normalized to *β-actin* or *GAPDH* (see figures or figure legends) and calculated using the $\Delta\,\Delta^{Ct}$ method. See Supplementary Methods for full list of primers used.

Western blot

See Supplementary Methods for details.

Cells proliferation assay

Ki-67 labeling assay and cell number counting assay were used to assess the proliferation capacity of BMECs following myelin debris engulfment. See Supplementary Methods for detailed information.

***In vivo* Matrigel plug angiogenesis assay**

Matrigel plug angiogenesis assay was performed with a method modified from our previous publication [59]. Briefly, 8×10^5 primary myelin-BMECs or naïve BMECs were mixed with 100 μl of pre-cooled Matrigel solution. The mixtures were subcutaneously injected in mice. Myelin-ECs, naïve-ECs and PBS (as blank control) were injected in the same mouse at different sites. After implantation for 7 days, the Matrigel plugs were excised, immediately photographed with a MVX10 Macro Zoom microscope (Olympus), subsequently followed by regular tissue histology and immunofluorescent staining for CD31 to label microvessels, whose density was analyzed and calculated as the percentage of CD31 positive area to the whole field.

BMDMϕ adhesion on endothelial cells

BDECs were seeded in 24-well plates and treated with or without 1mg/ml CFSE-labeled myelin debris for 72 hr to induce myelin-ECs. After removal of the myelin debris remnant in the culture, 3×10^5 BMDMϕ were added to naive-ECs and myelin-ECs monolayer. After 1 hr adhesion, non-adhered BMDMϕ were gently washed away with PBS for 5 times. The adhered BMDMϕ on EC monolayer were stained with Mac-2 antibody and imaged by a combination of phase contrast and fluorescent microscopy for visualization of endothelial monolayer and Mac-2^+ BMDMϕ, respectively. The number of Mac-2^+ BMDMϕ that adhered on endothelial monolayer was counted and normalized to the number of ECs as the percentage of BMDMϕ adhesion onto endothelial monolayer. See Supplementary Methods for more information.

BMDMϕ chemotaxis towards endothelial cells supernatant

A modified transwell assay was used to examine BMDMϕ chemotaxis towards EC's supernatant. After BMECs engulf myelin debris for three days, they were quickly washed with PBS three times. This step gets rid of most remaining non-engulfed myelin debris in ECs. After the washes, myelin-ECs were cultured for 24 hr in fresh culture media, followed by collection of cell culture supernatant from the myelin-ECs. The cell culture supernatant was clarified by centrifugation to remove any remaining myelin debris. Then, the BMEC supernatant was placed in the bottom chamber of the transwell, and BMDMϕ were seeded on the upper chamber. After chemotaxis for 6 hr, migrated BMDMϕ on the lower side of the membrane were stained with crystal violet (Alfa Aesar).

Astrocytes-endothelial cells co-culture assay

Primary astrocytes were isolated from C57BL/6 mice between 2 and 3 days old [60]. For astrocyte-EC co-culture, we used a transwell system where astrocytes were seeded in the lower chamber and BMECs were seeded in the upper chamber. See Supplementary Methods for detailed information.

***In vitro* endothelial-to-mesenchymal transition (endoMT) assay**

Myelin debris (1mg/ml) was added to BMECs for 1, 3, 5, 7, and 10 days and culture medium was changed every 3 days, followed by morphological observation of spindle-shape cells. BMECs were considered spindle-shaped when the diameter at their longest axis to be 1.5-fold greater than the average diameter of untreated cobblestone BMECs. See Supplementary Methods for detailed information.

Spinal cord BMEC injection

Myelin-laden BMECs (myelin-ECs) were generated by treatment with myelin debris for 72 hr, followed by wash to remove non-ingested myelin debris. Both control BMECs (naïve-ECs) and myelin-ECs were fluorescently labeled after incubation for 1 hr with 50 μM CFSE in DMEM without serum and washed once with PBS containing 100 mM glycine and twice with PBS. The cells were trypinsized and resuspended in cold PBS. The CFSE signals in naïve-ECs and myelin-ECs were confirmed after labeling. The fluorescent intensity of CFSE in myelin-ECs were much more rapidly diluted than naïve-ECs after subculture (data not shown), probably due to robust proliferation of myelin-ECs, as shown in Fig. 5. BMECs at 1×10^5 in 0.5 μl were injected in T10 spinal cords of normal mice using a 33 gauge needle attached to Hamilton syringe. 0.5 μl PBS injection was included as blank control. Myelin debris in 0.5 μl injection was included as a control to illustrate whether or not myelin debris, without ECs uptake, could elicit any responses when compared to myelin-EC injection. ECs cultured with myelin debris in the presence of 70°C heated serum (IgG-inactivated), which demonstrated that myelin debris contacted ECs without being internalized, were included to illustrate whether or not blocking EC myelin uptake could abrogate any *in vivo* spinal cord responses induced by myelin-ECs. The spinal cords were minimally exposed to avoid strong mechanical injury that may cause any unfavorable interference with cell injection. After 7 days of injection, mice were anaesthetized and perfused, followed by collection of spinal cords for regular histology and immunostaining..

Statistical analysis

Data distribution was assumed to be normal but this was not formally tested. The statistical significance of the difference between control and experimental groups was determined by two-sided Student's *t*-test, unless otherwise indicated, using Prism 7 (Graphpad, San Diego, CA). Differences were considered statistically significant when $p<0.05$. * denotes $p<0.05$, ** for $p<0.01$, *** for $p<0.001$ and **** for $p<0.0001$ as shown in figures and figure legends. Data were shown as mean ± s.e.m unless otherwise indicated.

Reporting Summary

Further information on research design is available in the Nature Research Reporting Summary linked to this article.

Data availability

All data supporting the findings of the current study are available from the corresponding authors upon request.

Methods-only References

47. Young, W. Spinal cord contusion models. *Prog Brain Res* **137**, 231-255 (2002).

48. Wu, H.*, et al.* Caveolin-1 Is Critical for Lymphocyte Trafficking into Central Nervous System during Experimental Autoimmune Encephalomyelitis. *The Journal of neuroscience : the official journal of the Society for Neuroscience* **36**, 5193-5199 (2016).

49. Mi, S.*, et al.* LINGO-1 antagonist promotes spinal cord remyelination and axonal integrity in MOG-induced experimental autoimmune encephalomyelitis. *Nature medicine* **13**, 1228-1233 (2007).

50. Gitik, M., Liraz-Zaltsman, S., Oldenborg, P.A., Reichert, F. & Rotshenker, S. Myelin down-regulates myelin phagocytosis by microglia and macrophages through interactions between CD47 on myelin and SIRPalpha (signal regulatory protein-alpha) on phagocytes. *J Neuroinflammation* **8**, 24 (2011).

51. Hackett, A.R.*, et al.* STAT3 and SOCS3 regulate NG2 cell proliferation and differentiation after contusive spinal cord injury. *Neurobiology of disease* **89**, 10-22 (2016).

52. Bolger, A.M., Lohse, M. & Usadel, B. Trimmomatic: a flexible trimmer for Illumina sequence data. *Bioinformatics* **30**, 2114-2120 (2014).

53. Kim, D.*, et al.* TopHat2: accurate alignment of transcriptomes in the presence of insertions, deletions and gene fusions. *Genome biology* **14**, R36 (2013).

54. Li, H.*, et al.* The Sequence Alignment/Map format and SAMtools. *Bioinformatics* **25**, 2078-2079 (2009).

55. Anders, S., Pyl, P.T. & Huber, W. HTSeq--a Python framework to work with high-throughput sequencing data. *Bioinformatics* **31**, 166-169 (2015).

56. Love, M.I., Huber, W. & Anders, S. Moderated estimation of fold change and dispersion for RNA-seq data with DESeq2. *Genome biology* **15**, 550 (2014).

57. Wu, H., Wang, C. & Wu, Z. A new shrinkage estimator for dispersion improves differential expression detection in RNA-seq data. *Biostatistics* **14** (2013).

58. Benjamini, Y. & Hochberg, Y. Controlling the false discovery rate: a practical and powerful approach to multiple testing. *J R Stat Soc Ser B Methodol* **57** (1995).

59. Wang, X.*, et al.* MIF produced by bone marrow-derived macrophages contributes to teratoma progression after embryonic stem cell transplantation. *Cancer Res* **72**, 2867-2878 (2012).

60. Wu, J., Wrathall, J.R. & Schachner, M. Phosphatidylinositol 3-kinase/protein kinase Cdelta activation induces close homolog of adhesion molecule L1 (CHL1) expression in cultured astrocytes. *Glia* **58**, 315-328 (2010).

Figure 1.

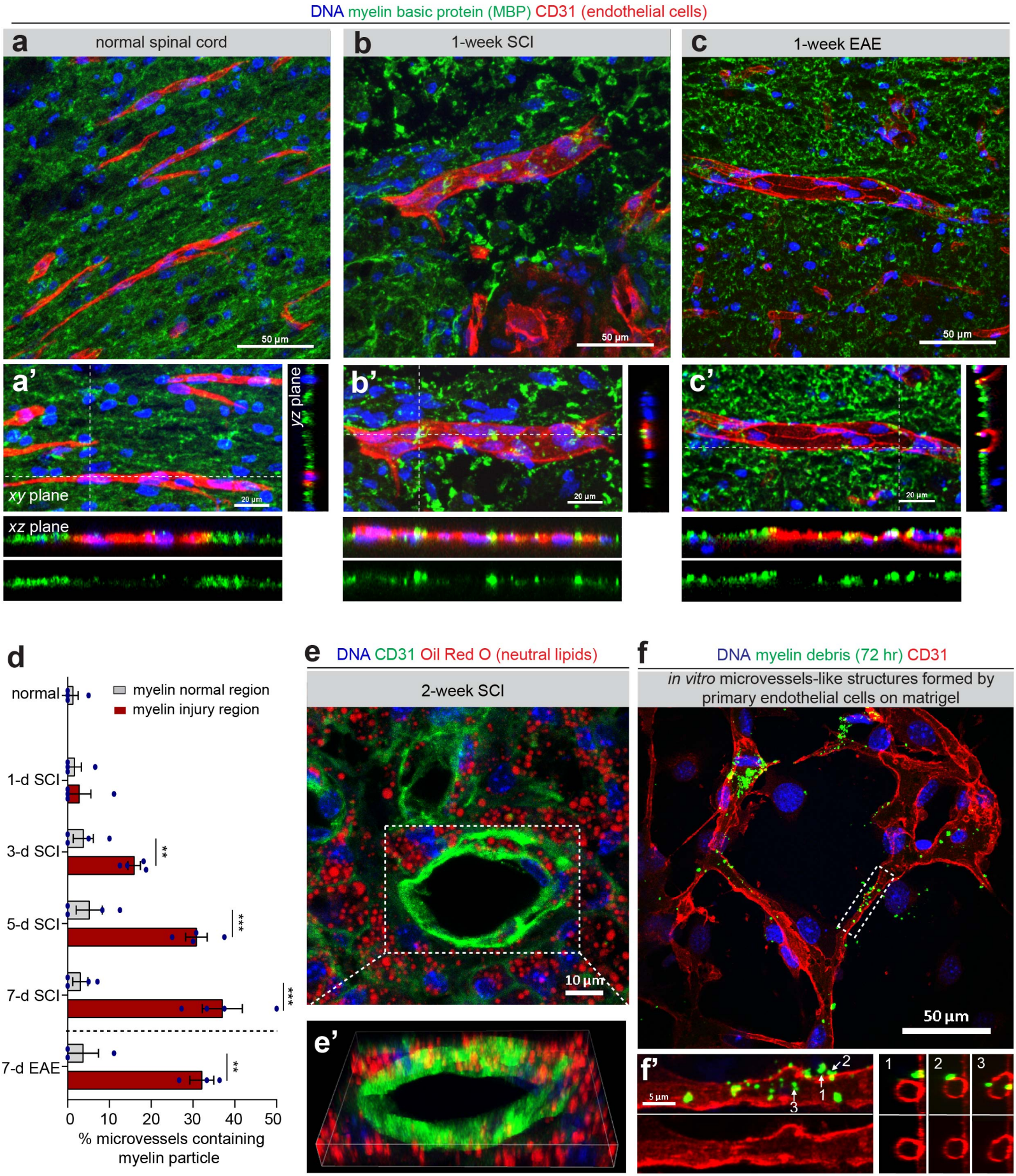
DNA myelin basic protein (MBP) CD31 (endothelial cells)
a
normal spinal cord
b
1-week SCI
c
1-week EAE
50 µm
a'
b'
c'
yz plane
xy plane
xz plane
20 µm
d
normal
myelin normal region
myelin injury region
1-d SCI
3-d SCI
5-d SCI
7-d SCI
7-d EAE
**
***
0
10
20
30
40
50
% microvessels containing myelin particle
e
DNA CD31 Oil Red O (neutral lipids)
2-week SCI
10 µm
e'
f
DNA myelin debris (72 hr) CD31
in vitro microvessels-like structures formed by primary endothelial cells on matrigel
50 µm
f'
5 µm
1
2
3

Figure 2.

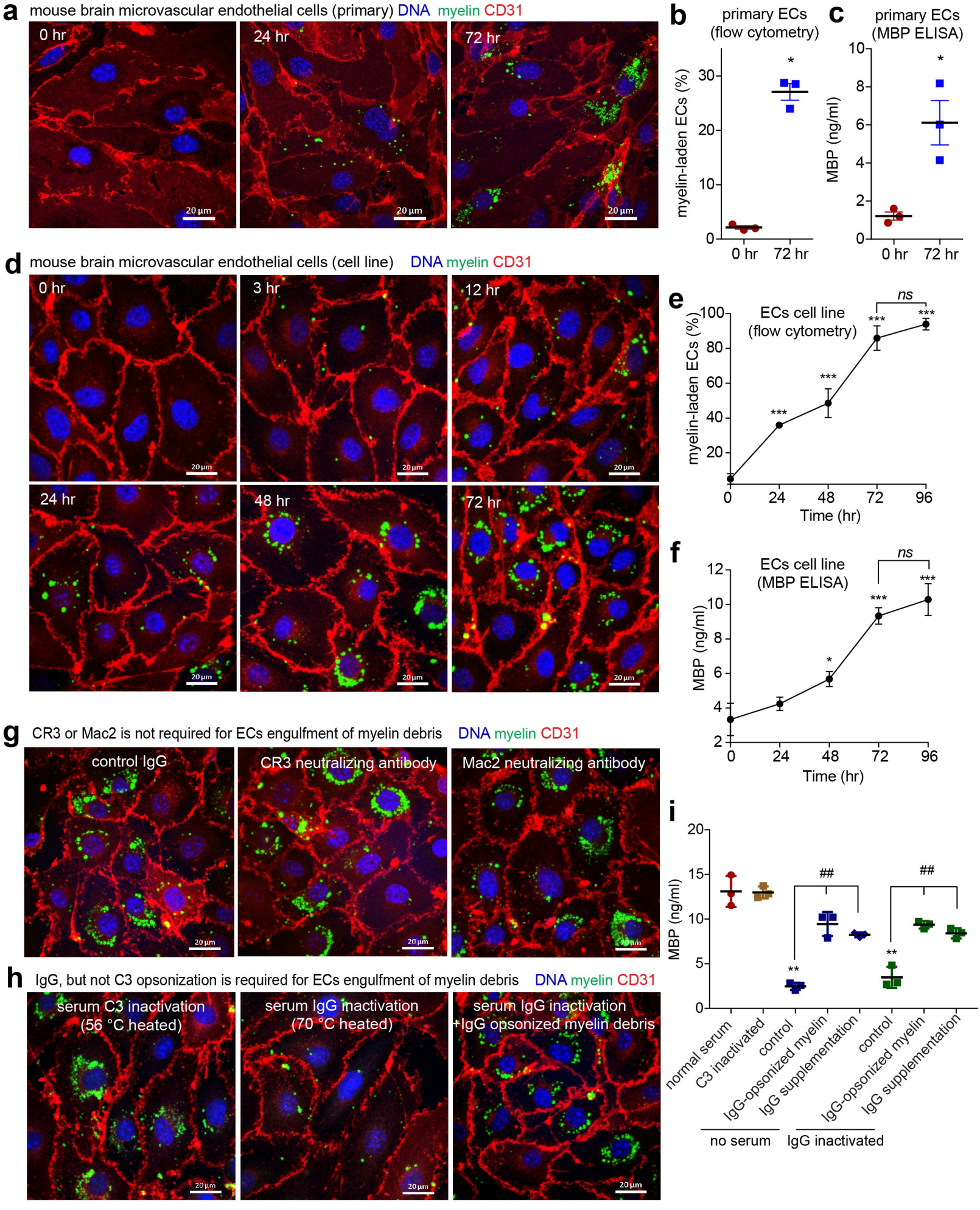
a
mouse brain microvascular endothelial cells (primary) DNA myelin CD31
0 hr
24 hr
72 hr
20 μm
b
primary ECs (flow cytometry)
myelin-laden ECs (%)
0 hr
72 hr
c
primary ECs (MBP ELISA)
MBP (ng/ml)
d
mouse brain microvascular endothelial cells (cell line) DNA myelin CD31
0 hr
3 hr
12 hr
24 hr
48 hr
72 hr
e
ECs cell line (flow cytometry)
myelin-laden ECs (%)
Time (hr)
ns
f
ECs cell line (MBP ELISA)
MBP (ng/ml)
Time (hr)
g
CR3 or Mac2 is not required for ECs engulfment of myelin debris DNA myelin CD31
control IgG
CR3 neutralizing antibody
Mac2 neutralizing antibody
h
IgG, but not C3 opsonization is required for ECs engulfment of myelin debris DNA myelin CD31
serum C3 inactivation (56 °C heated)
serum IgG inactivation (70 °C heated)
serum IgG inactivation +IgG opsonized myelin debris
i
MBP (ng/ml)
normal serum
C3 inactivated
control
IgG-opsonized myelin
IgG supplementation
control
IgG-opsonized myelin
IgG supplementation
no serum
IgG inactivated

Figure 3.

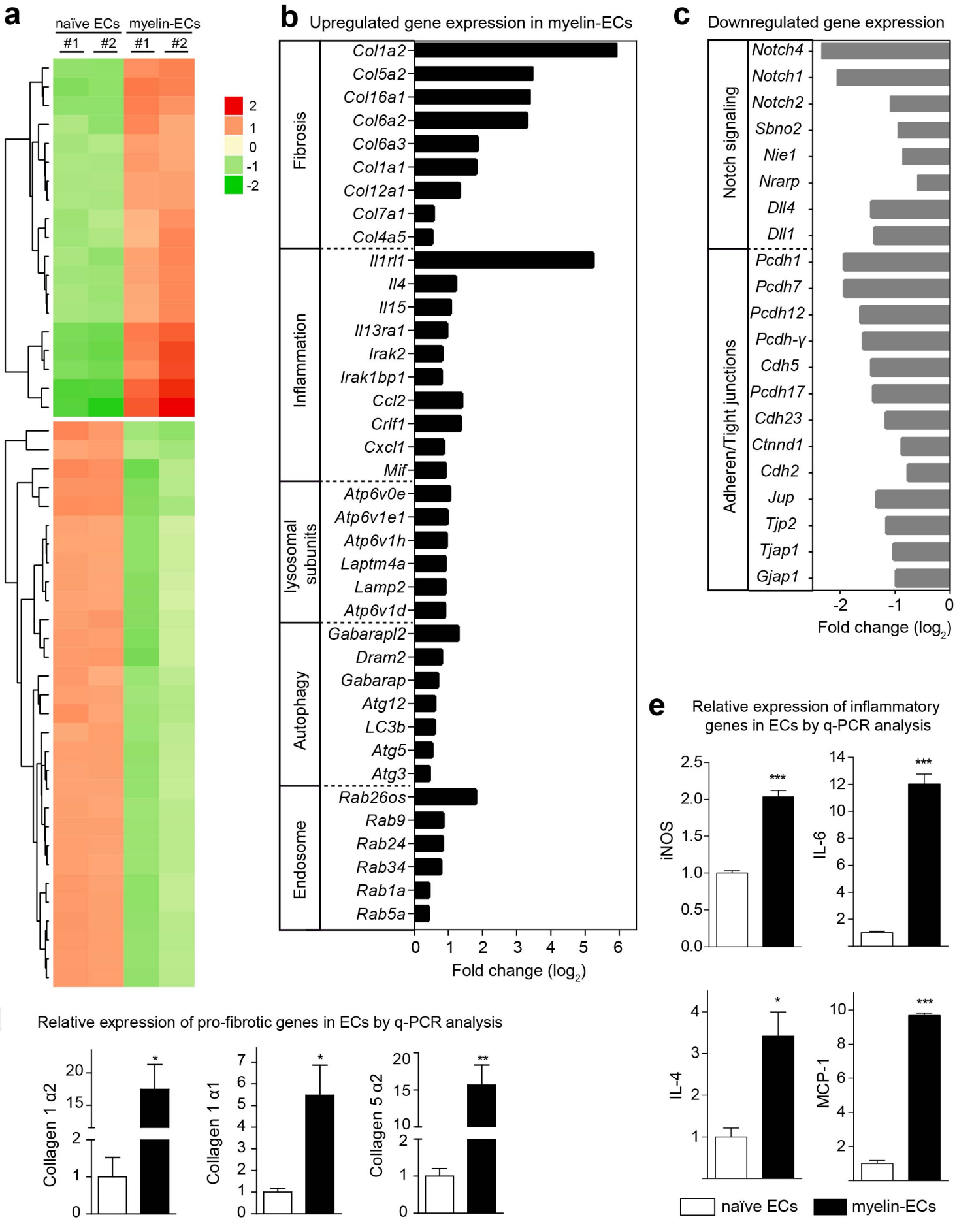
a
naïve ECs
myelin-ECs
#1
#2
#1
#2
2
1
0
-1
-2
b
Upregulated gene expression in myelin-ECs
Fibrosis
Col1a2
Col5a2
Col16a1
Col6a2
Col6a3
Col1a1
Col12a1
Col7a1
Col4a5
Inflammation
Il1rl1
Il4
Il15
Il13ra1
Irak2
Irak1bp1
Ccl2
Crlf1
Cxcl1
Mif
lysosomal subunits
Atp6v0e
Atp6v1e1
Atp6v1h
Laptm4a
Lamp2
Atp6v1d
Autophagy
Gabarapl2
Dram2
Gabarap
Atg12
LC3b
Atg5
Atg3
Endosome
Rab26os
Rab9
Rab24
Rab34
Rab1a
Rab5a
0 1 2 3 4 5 6
Fold change (log2)
c
Downregulated gene expression
Notch signaling
Notch4
Notch1
Notch2
Sbno2
Nie1
Nrarp
Dll4
Dll1
Adheren/Tight junctions
Pcdh1
Pcdh7
Pcdh12
Pcdh-γ
Cdh5
Pcdh17
Cdh23
Ctnnd1
Cdh2
Jup
Tjp2
Tjap1
Gjap1
-2 -1 0
Fold change (log2)
d
Relative expression of pro-fibrotic genes in ECs by q-PCR analysis
Collagen 1 α2
Collagen 1 α1
Collagen 5 α2
e
Relative expression of inflammatory genes in ECs by q-PCR analysis
iNOS
IL-6
IL-4
MCP-1
naïve ECs
myelin-ECs

Figure 4.

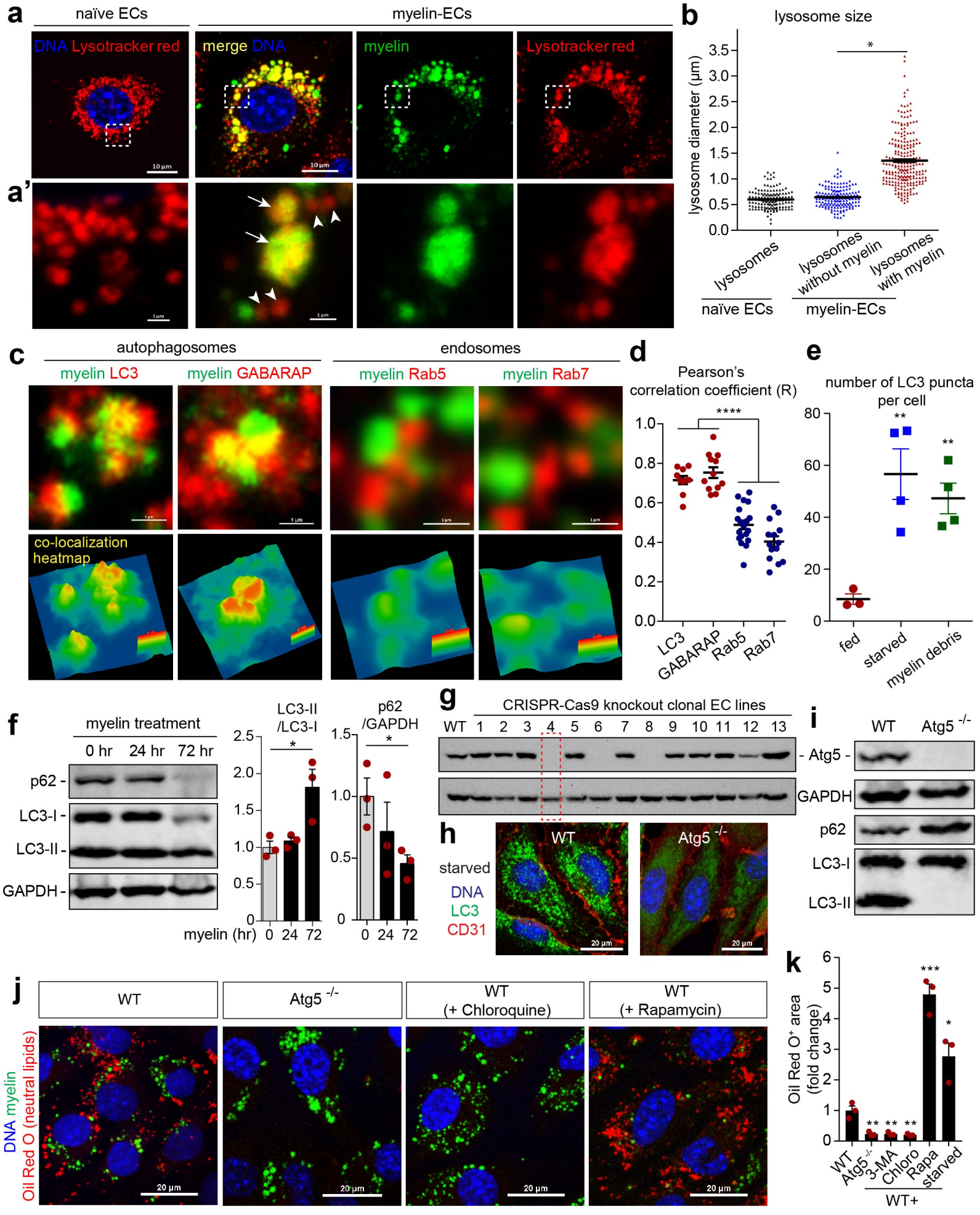
a
naïve ECs
myelin-ECs
DNA Lysotracker red
merge DNA
myelin
Lysotracker red
a'
b
lysosome size
lysosome diameter (μm)
lysosomes
lysosomes without myelin
lysosomes with myelin
naïve ECs
myelin-ECs
c
autophagosomes
endosomes
myelin LC3
myelin GABARAP
myelin Rab5
myelin Rab7
co-localization heatmap
d
Pearson's correlation coefficient (R)
LC3
GABARAP
Rab5
Rab7
e
number of LC3 puncta per cell
fed
starved
myelin debris
f
myelin treatment
0 hr
24 hr
72 hr
p62
LC3-I
LC3-II
GAPDH
LC3-II /LC3-I
p62 /GAPDH
myelin (hr)
g
CRISPR-Cas9 knockout clonal EC lines
WT
h
starved
DNA
LC3
CD31
Atg5 -/-
i
Atg5 -/-
Atg5
j
WT
Atg5 -/-
WT (+ Chloroquine)
WT (+ Rapamycin)
DNA myelin
Oil Red O (neutral lipids)
k
Oil Red O+ area (fold change)
WT
Atg5-/-
3-MA
Chloro
Rapa
starved
WT+

Figure 5.

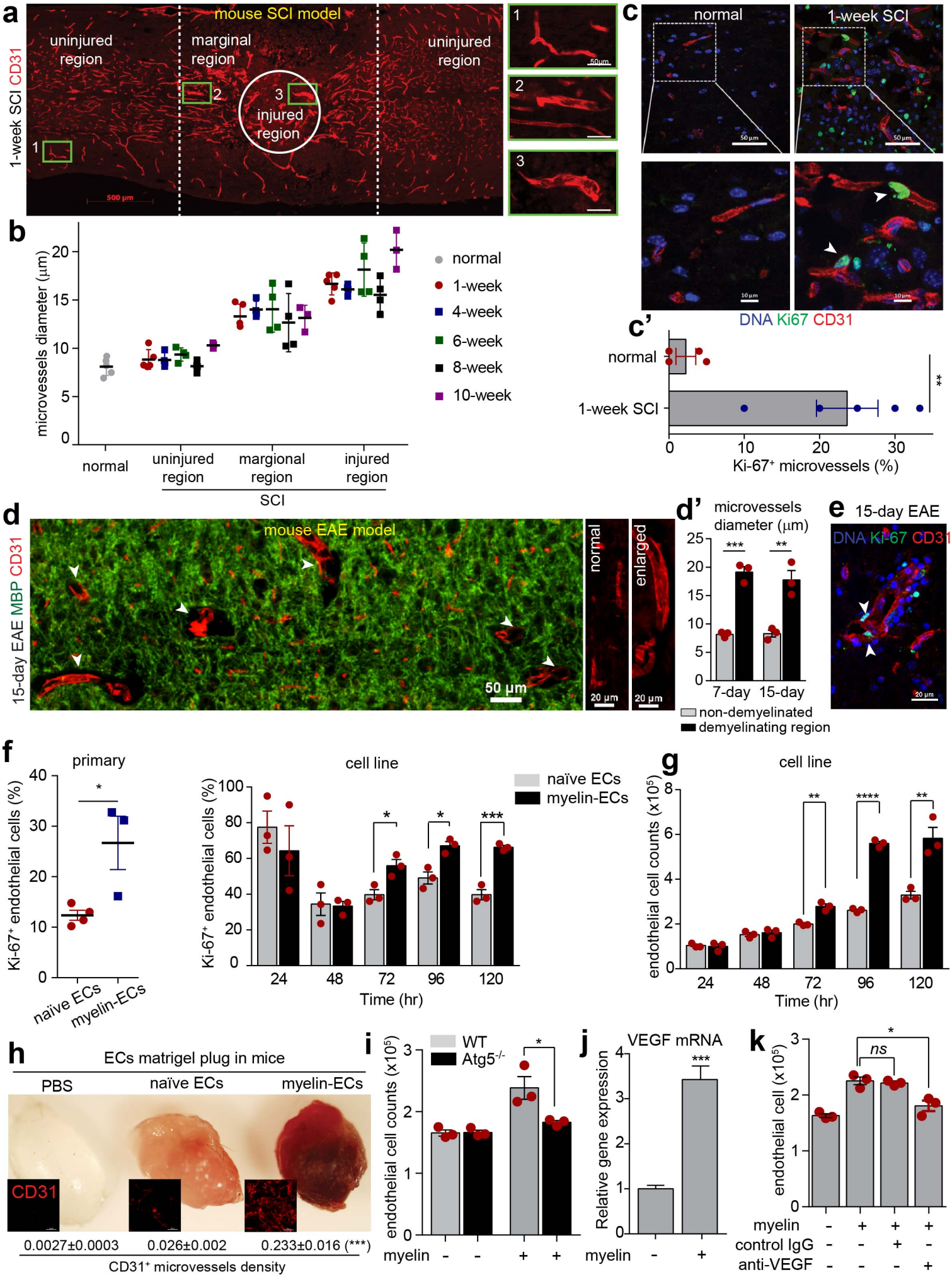
a
mouse SCI model
uninjured region
marginal region
injured region
1-week SCI CD31
b
microvessels diameter (μm)
normal
1-week
4-week
6-week
8-week
10-week
SCI
c
normal
1-week SCI
DNA Ki67 CD31
c'
Ki-67+ microvessels (%)
d
mouse EAE model
15-day EAE MBP CD31
d'
microvessels diameter (μm)
non-demyelinated
demyelinating region
e
15-day EAE
DNA Ki-67 CD31
f
primary
cell line
naïve ECs
myelin-ECs
Ki-67+ endothelial cells (%)
Time (hr)
g
endothelial cell counts (x10^5)
h
ECs matrigel plug in mice
PBS
naïve ECs
myelin-ECs
CD31
0.0027±0.0003
0.026±0.002
0.233±0.016 (***)
CD31+ microvessels density
i
WT
Atg5-/-
j
VEGF mRNA
Relative gene expression
k
ns
myelin
control IgG
anti-VEGF

Figure 6.

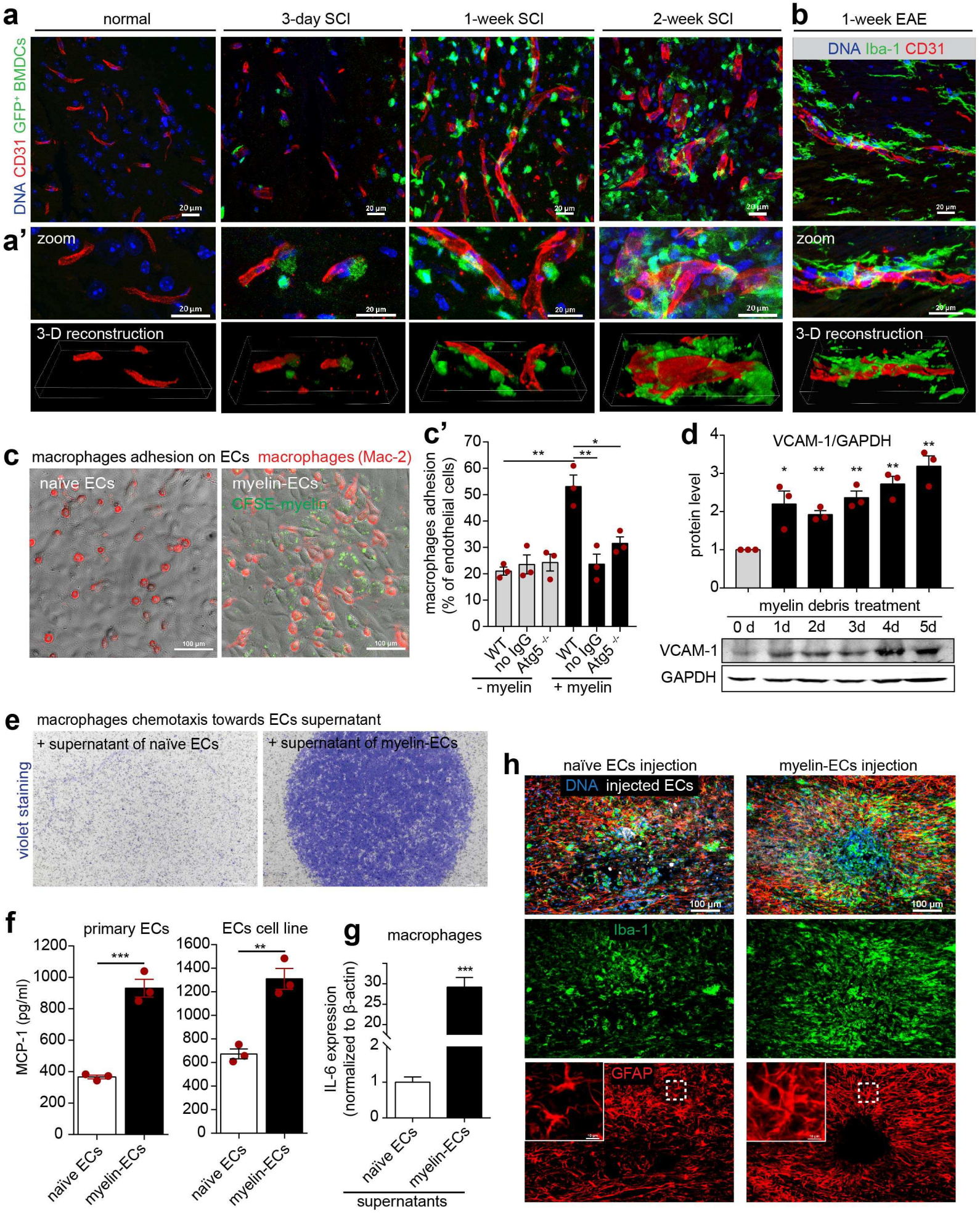
a
normal
3-day SCI
1-week SCI
2-week SCI
b
1-week EAE
DNA CD31 GFP+ BMDCs
DNA Iba-1 CD31
a'
zoom
3-D reconstruction
20 μm
c
macrophages adhesion on ECs
macrophages (Mac-2)
naïve ECs
myelin-ECs
CFSE-myelin
100 μm
c'
macrophages adhesion (% of endothelial cells)
WT
no IgG
Atg5 -/-
- myelin
+ myelin
d
VCAM-1/GAPDH
protein level
myelin debris treatment
0 d
1d
2d
3d
4d
5d
VCAM-1
GAPDH
e
macrophages chemotaxis towards ECs supernatant
+ supernatant of naïve ECs
+ supernatant of myelin-ECs
violet staining
f
primary ECs
ECs cell line
MCP-1 (pg/ml)
naïve ECs
myelin-ECs
g
macrophages
IL-6 expression (normalized to β-actin)
supernatants
h
naïve ECs injection
myelin-ECs injection
DNA injected ECs
Iba-1
GFAP

Figure 7.

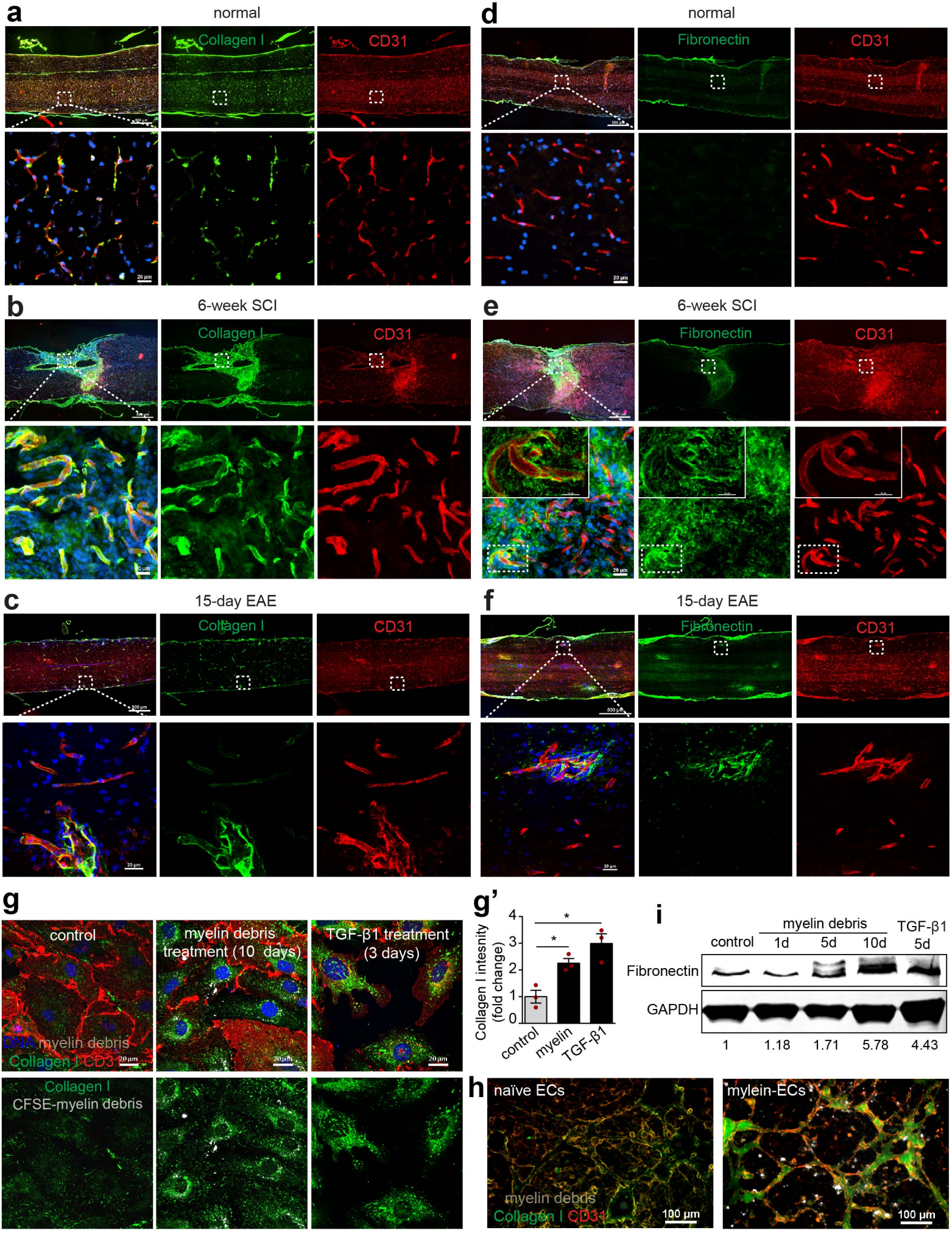
a
normal
Collagen I
CD31
d
normal
Fibronectin
CD31
b
6-week SCI
Collagen I
CD31
e
6-week SCI
Fibronectin
CD31
c
15-day EAE
Collagen I
CD31
f
15-day EAE
Fibronectin
CD31
g
control
myelin debris treatment (10 days)
TGF-β1 treatment (3 days)
DNA myelin debris
Collagen I CD31
Collagen I
CFSE-myelin debris
g'
Collagen I intesnity (fold change)
control
myelin
TGF-β1
i
myelin debris
control
1d
5d
10d
TGF-β1 5d
Fibronectin
GAPDH
1
1.18
1.71
5.78
4.43
h
naïve ECs
myelin debris
Collagen I CD31
100 μm
mylein-ECs
100 μm

Figure 8.

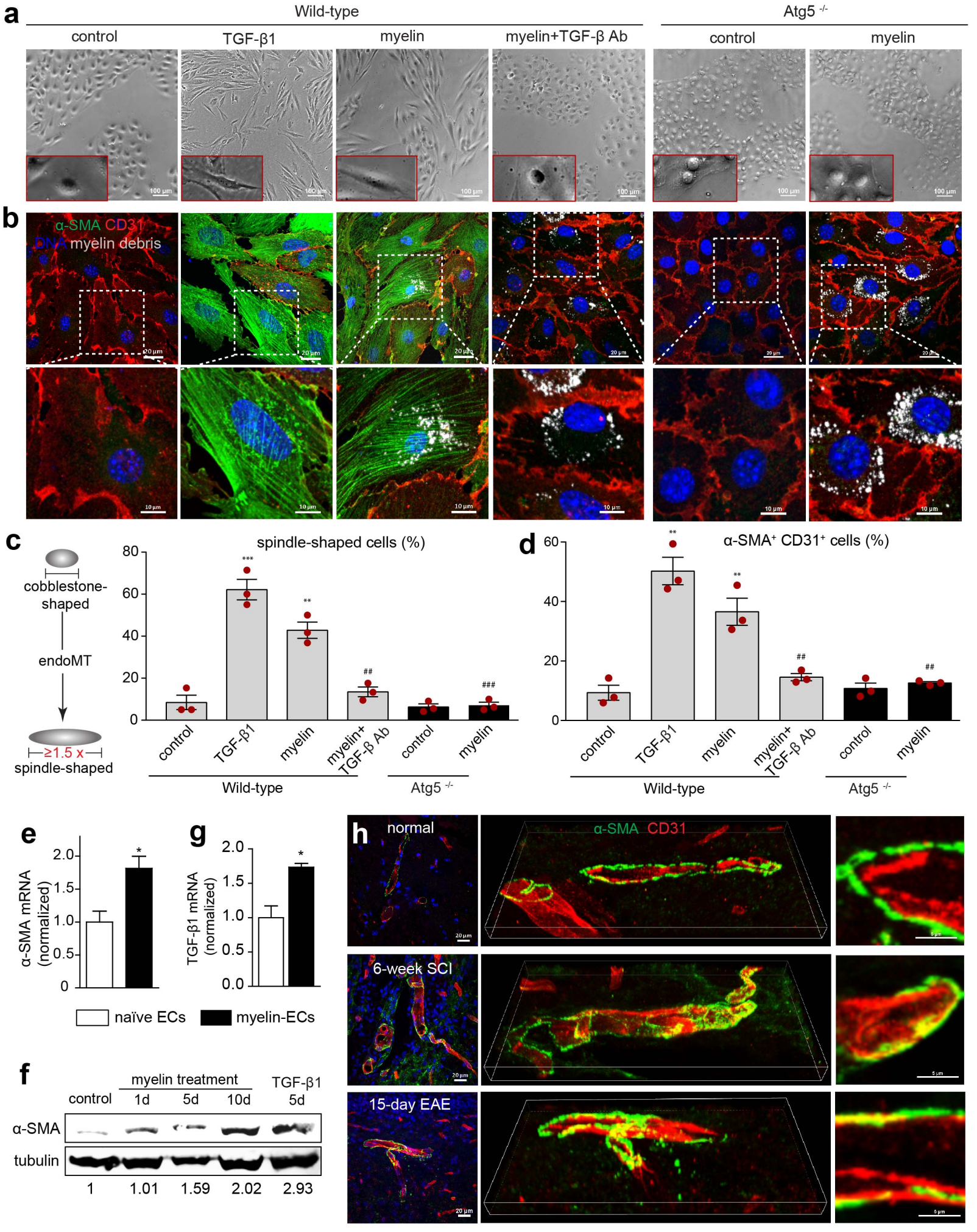
a
Wild-type
Atg5 -/-
control
TGF-β1
myelin
myelin+TGF-β Ab
control
myelin
b
α-SMA CD31
DNA myelin debris
c
cobblestone-shaped
endoMT
≥1.5 x
spindle-shaped
spindle-shaped cells (%)
control
TGF-β1
myelin
myelin+ TGF-β Ab
control
myelin
Wild-type
Atg5 -/-
d
α-SMA+ CD31+ cells (%)
control
TGF-β1
myelin
myelin+ TGF-β Ab
control
myelin
Wild-type
Atg5 -/-
e
α-SMA mRNA (normalized)
naïve ECs
myelin-ECs
g
TGF-β1 mRNA (normalized)
f
myelin treatment
control
1d
5d
10d
TGF-β1 5d
α-SMA
tubulin
1
1.01
1.59
2.02
2.93
h
normal
α-SMA CD31
6-week SCI
15-day EAE

Supplemental figure 1.

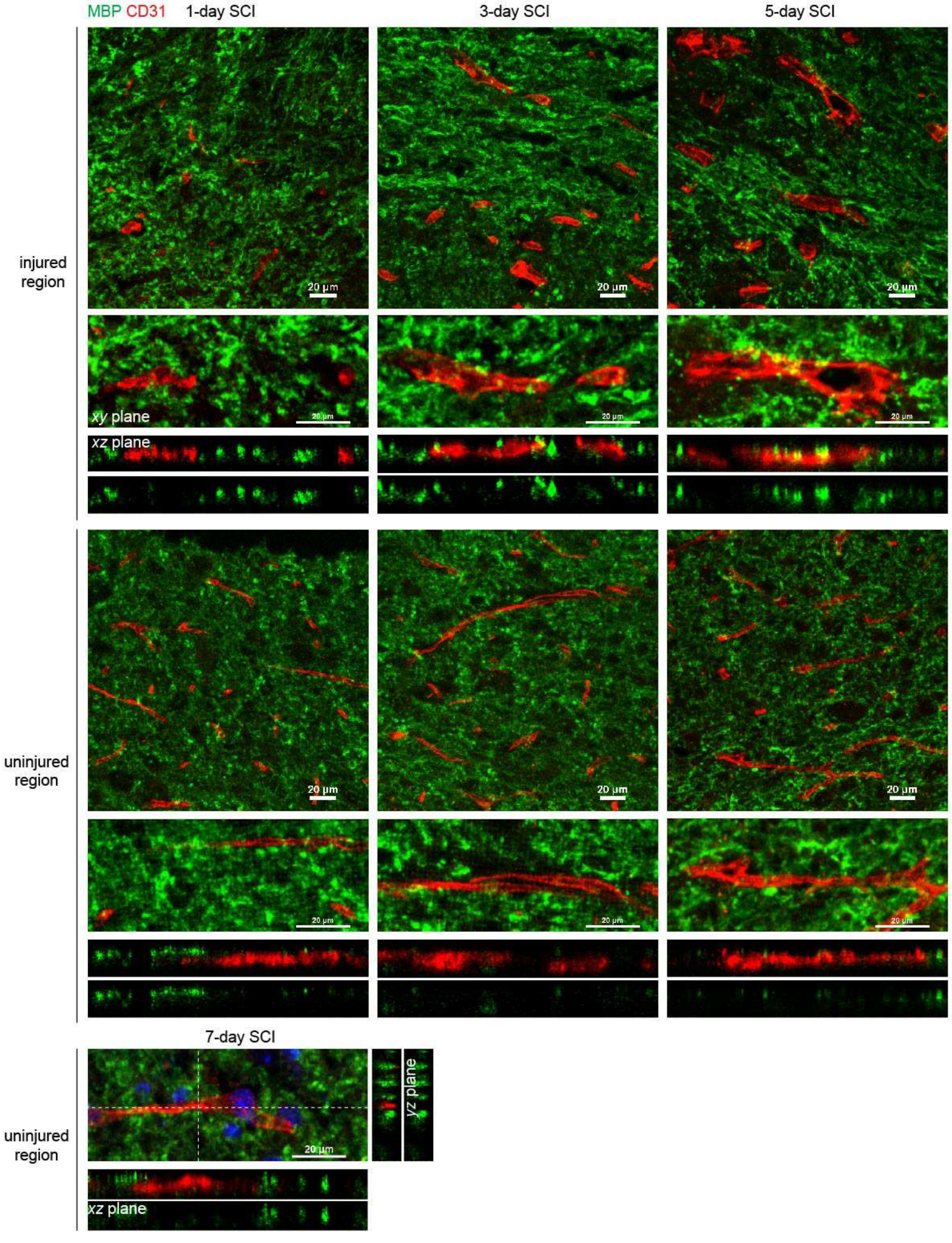

Supplemental figure 2.

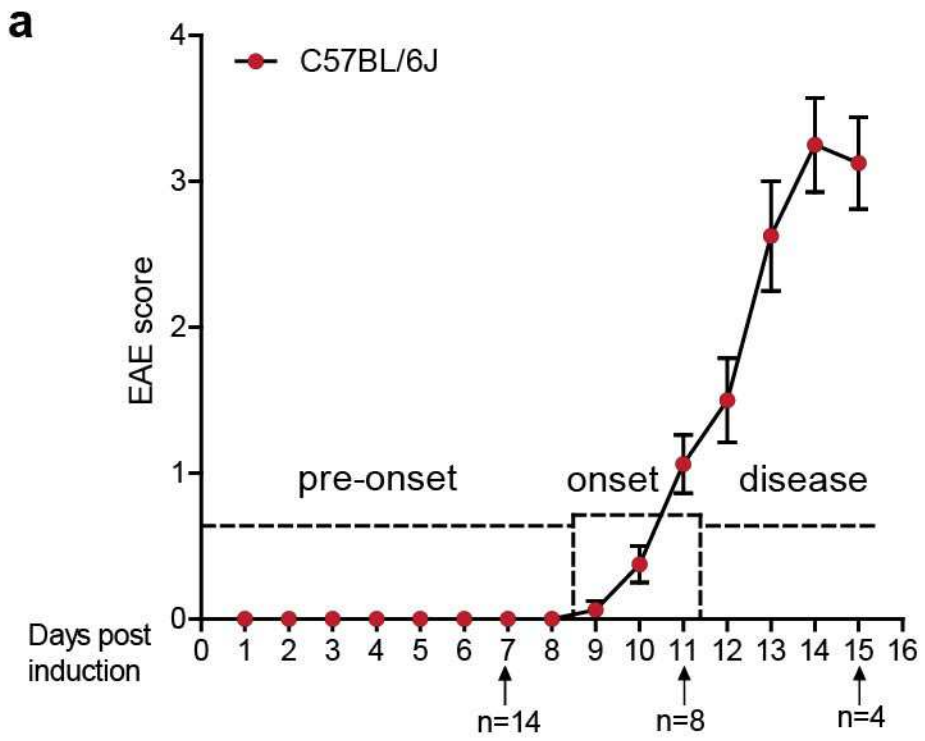

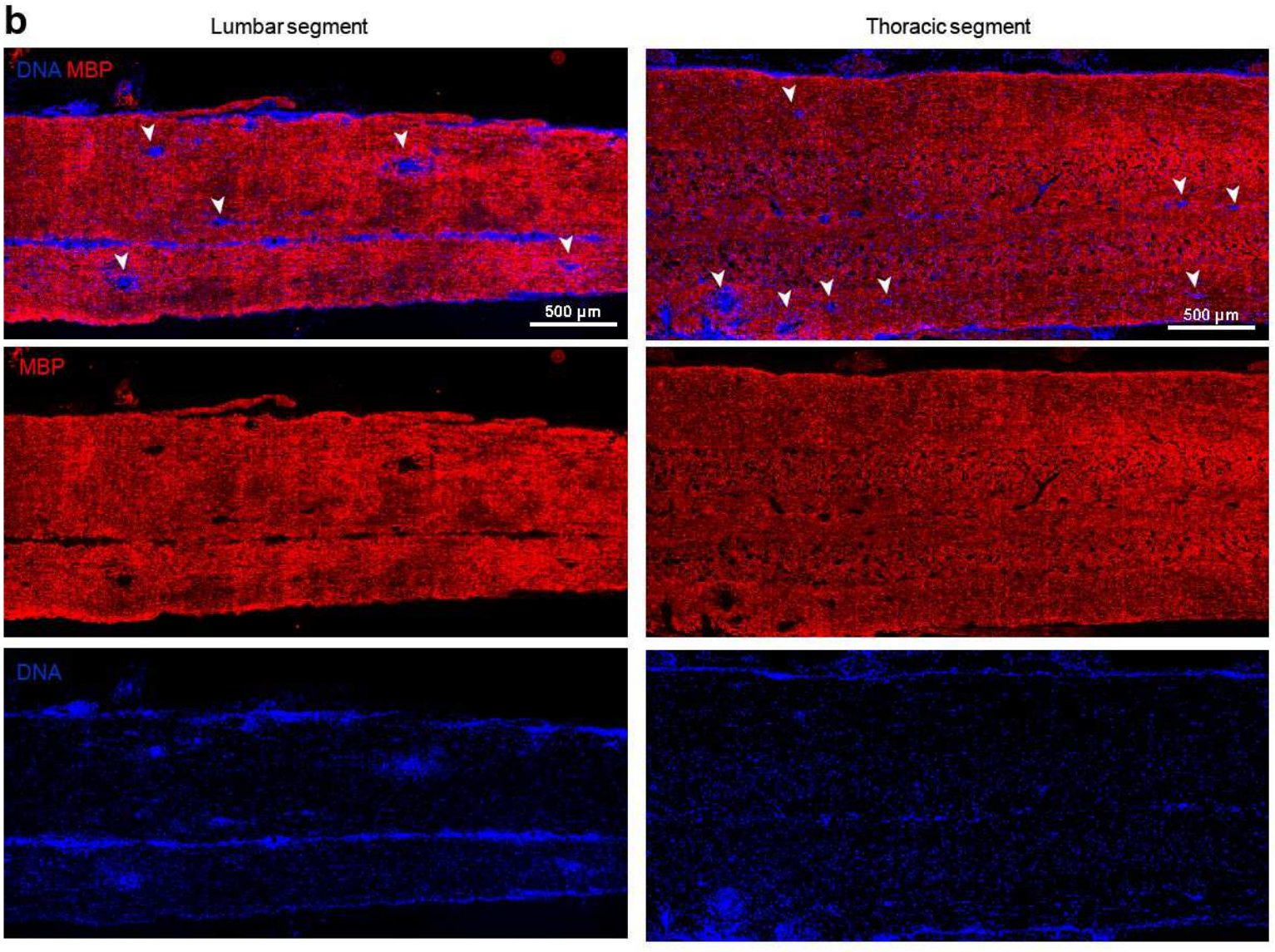

Supplemental figure 3

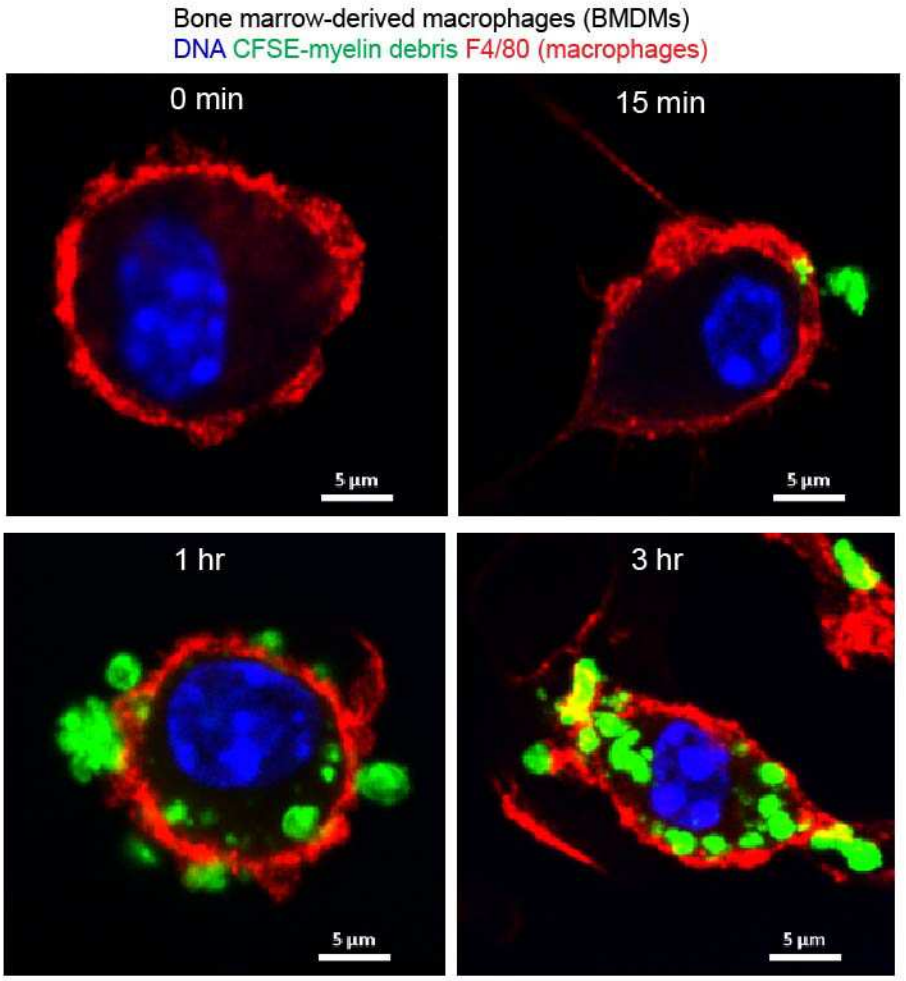

Supplemental figure 4.

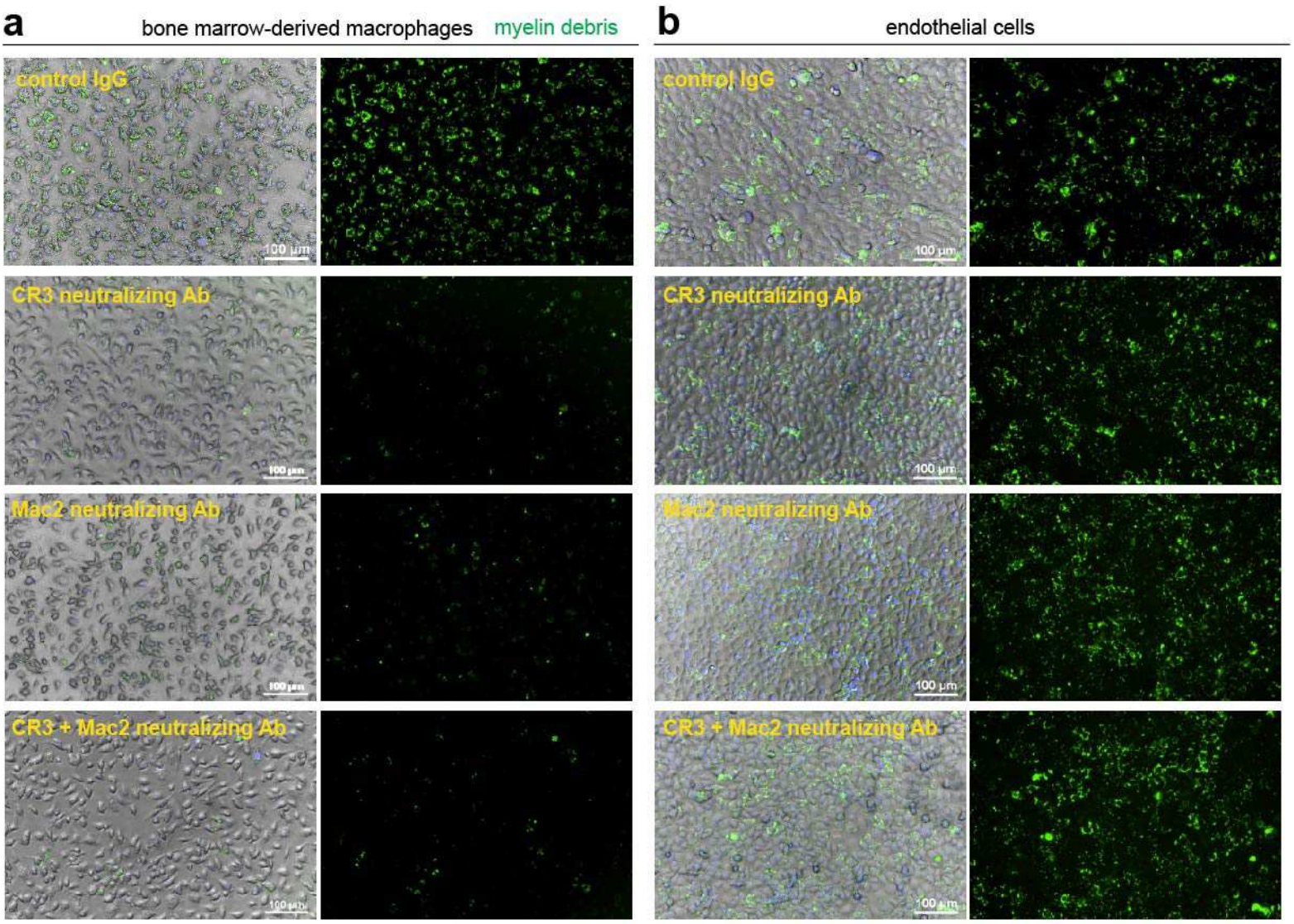

Supplemental figure 5.

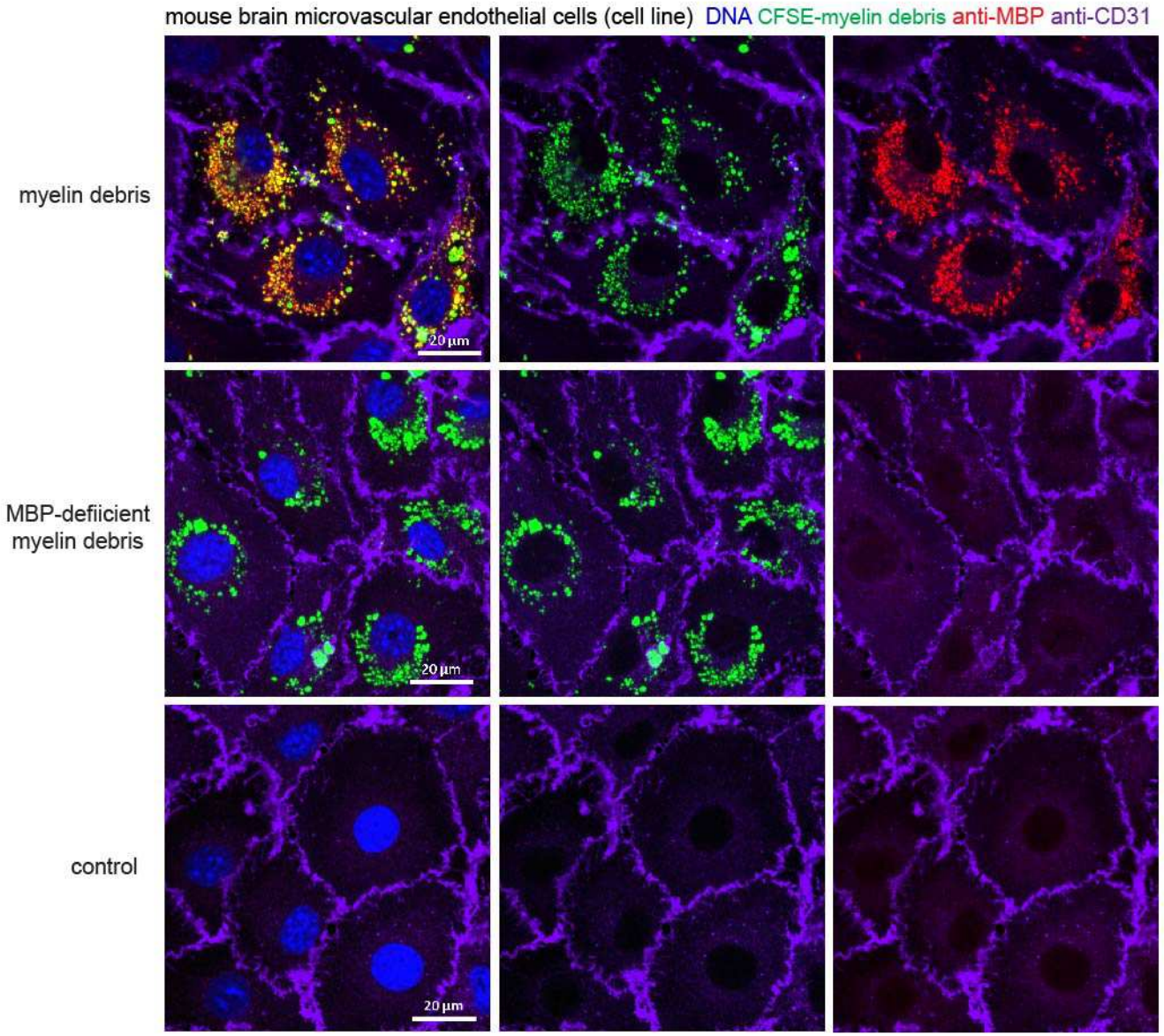

Supplemental figure 6.

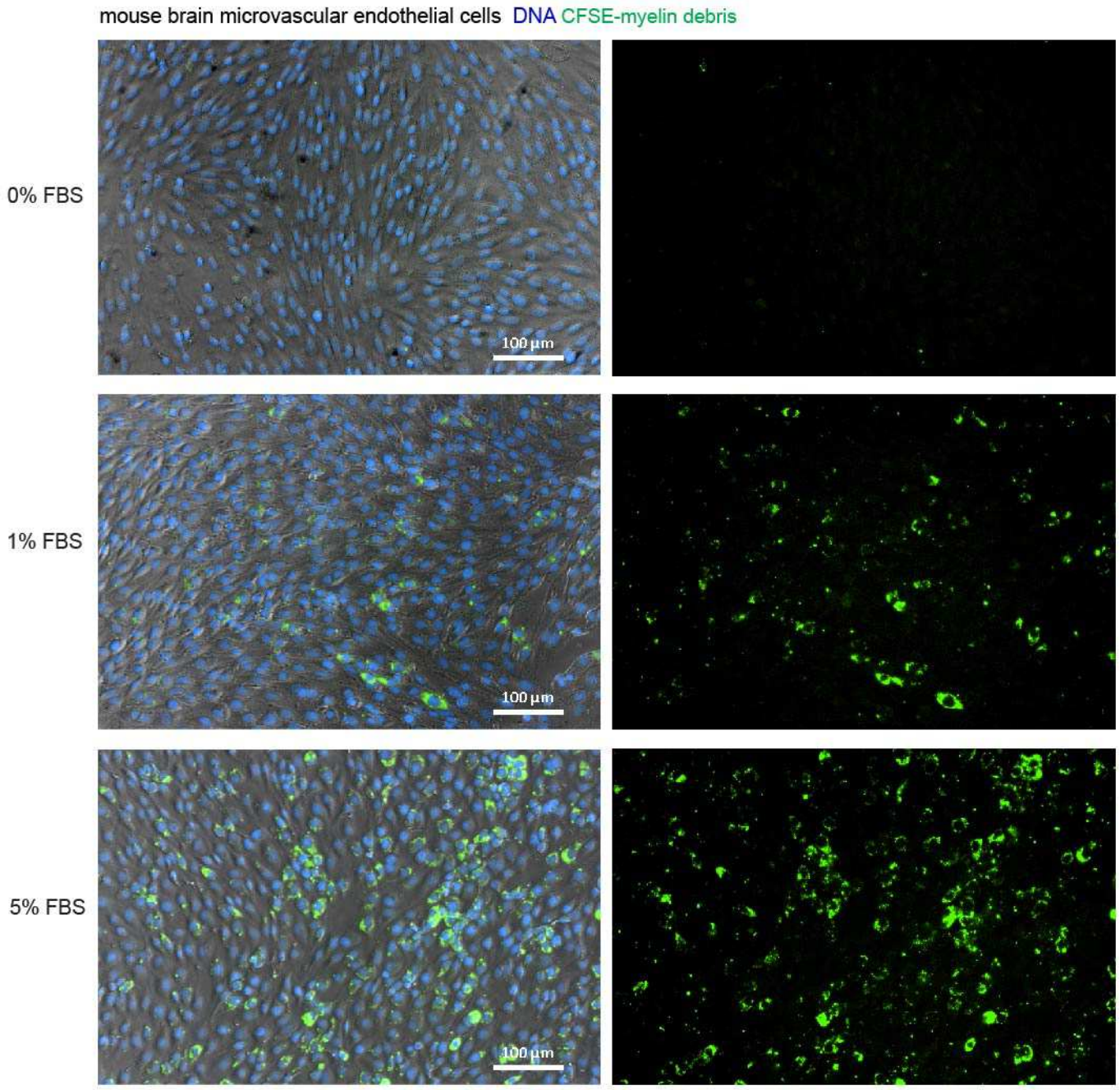

Supplemental figure 7.

a up-regulated

Pathway Name	Adj P
Metabolic pathways	4.69e-08
Protein digestion and absorption	9.22e-06
Focal adhesion	1.96e-05
ECM-receptor interaction	0.0001
Cytokine-cytokine receptor interaction	0.0014
Arachidonic acid metabolism	0.0014
Propanoate metabolism	0.0014
p53 signaling pathway	0.0024
Phagosome	0.0054
TGF-beta signaling pathway	0.0058
Allograft rejection	0.0062
Tight junction	0.0062
Hedgehog signaling pathway	0.0062
Glutathione metabolism	0.0062
MAPK signaling pathway	0.0084
Regulation of actin cytoskeleton	0.0103
Autoimmune thyroid disease	0.0108
Ribosome	0.0128
Melanoma	0.0128
Complement and coagulation cascades	0.0146
Salivary secretion	0.0148
Axon guidance	0.0160
Alzheimer's disease	0.0160
Pathways in cancer	0.0174
Pyruvate metabolism	0.0178

b down-regulated

Pathway Name	Adj P
Pathways in cancer	9.51e-23
Focal adhesion	1.97e-21
Regulation of actin cytoskeleton	2.08e-19
Endocytosis	2.12e-17
MAPK signaling pathway	3.84e-13
Axon guidance	1.66e-12
ECM-receptor interaction	2.38e-12
Adherens junction	2.38e-12
Notch signaling pathway	1.72e-09
GnRH signaling pathway	2.58e-09
ErbB signaling pathway	2.77e-09
Tight junction	8.26e-09
Arrhythmogenic right ventricular cardiomyopathy (ARVC)	1.98e-08
Calcium signaling pathway	1.98e-08
Phosphatidylinositol signaling system	3.81e-08
Wnt signaling pathway	4.56e-08
Bacterial invasion of epithelial cells	9.35e-08
Small cell lung cancer	1.31e-07
Amoebiasis	1.31e-07
Dilated cardiomyopathy	1.62e-07
Protein processing in endoplasmic reticulum	1.62e-07
Fc gamma R-mediated phagocytosis	1.77e-07
Insulin signaling pathway	1.85e-07
Hypertrophic cardiomyopathy (HCM)	4.61e-07
ABC transporters	4.61e-07

Supplemental figure 8.

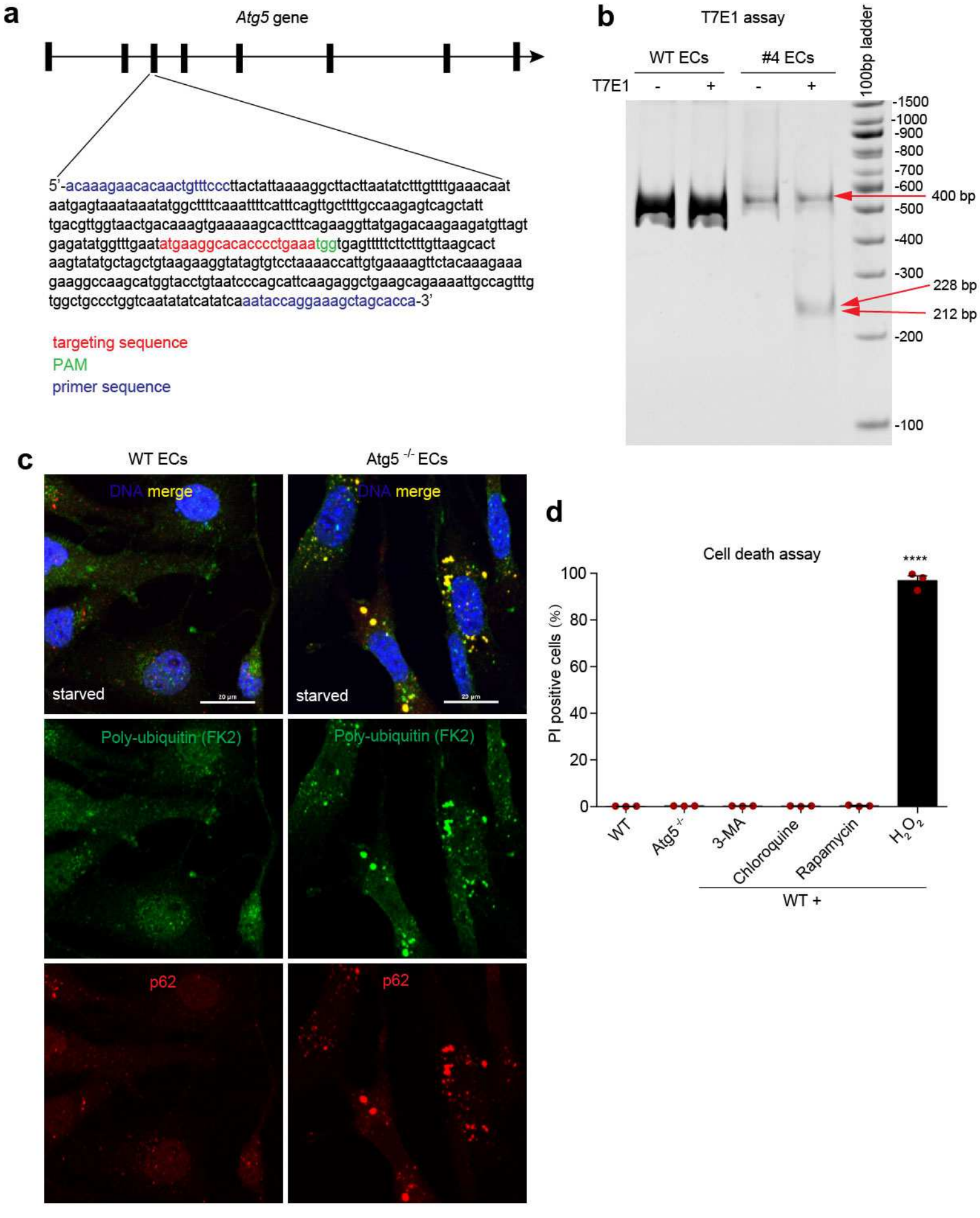

Supplemental figure 9.

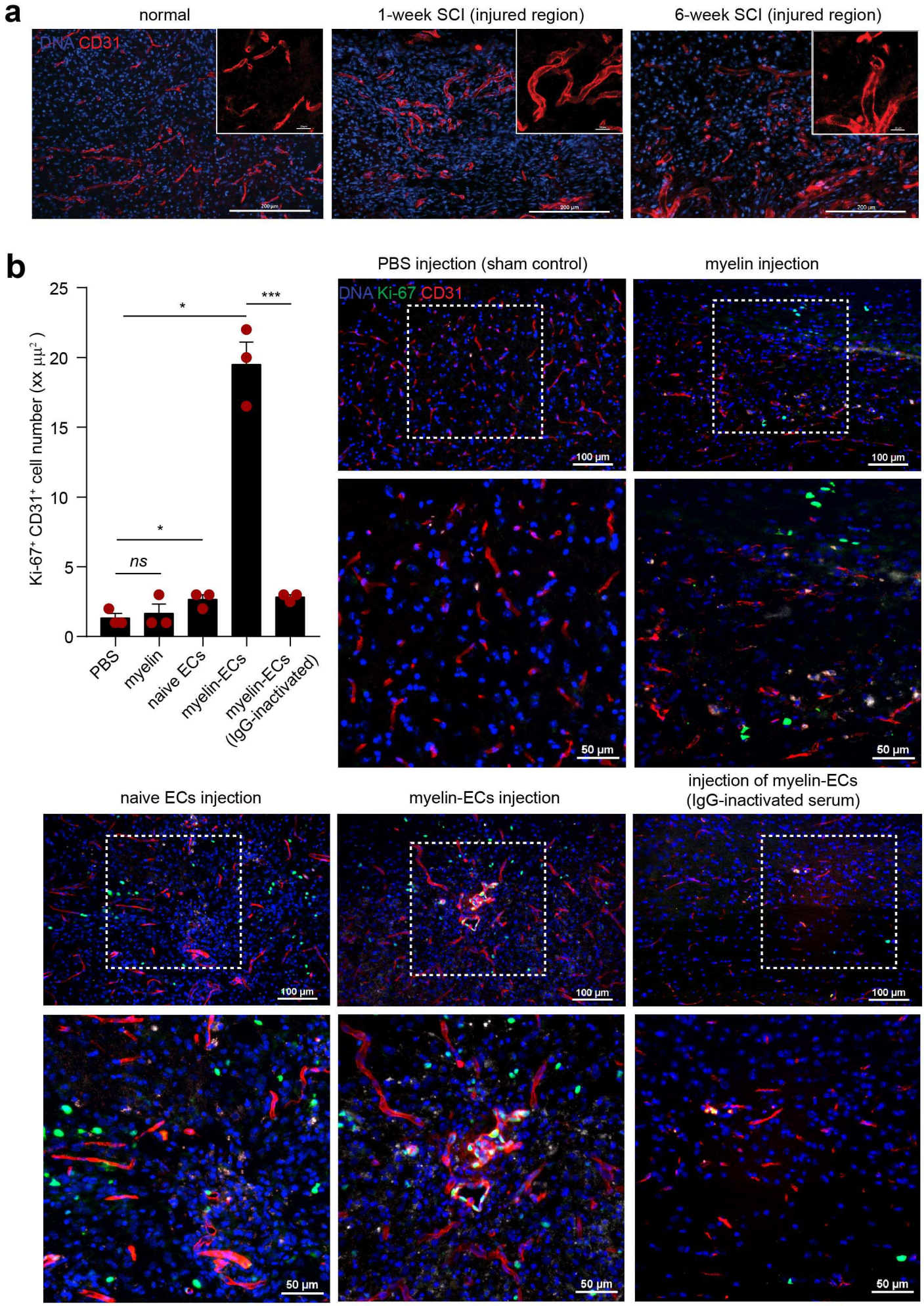

Supplemental figure 10.

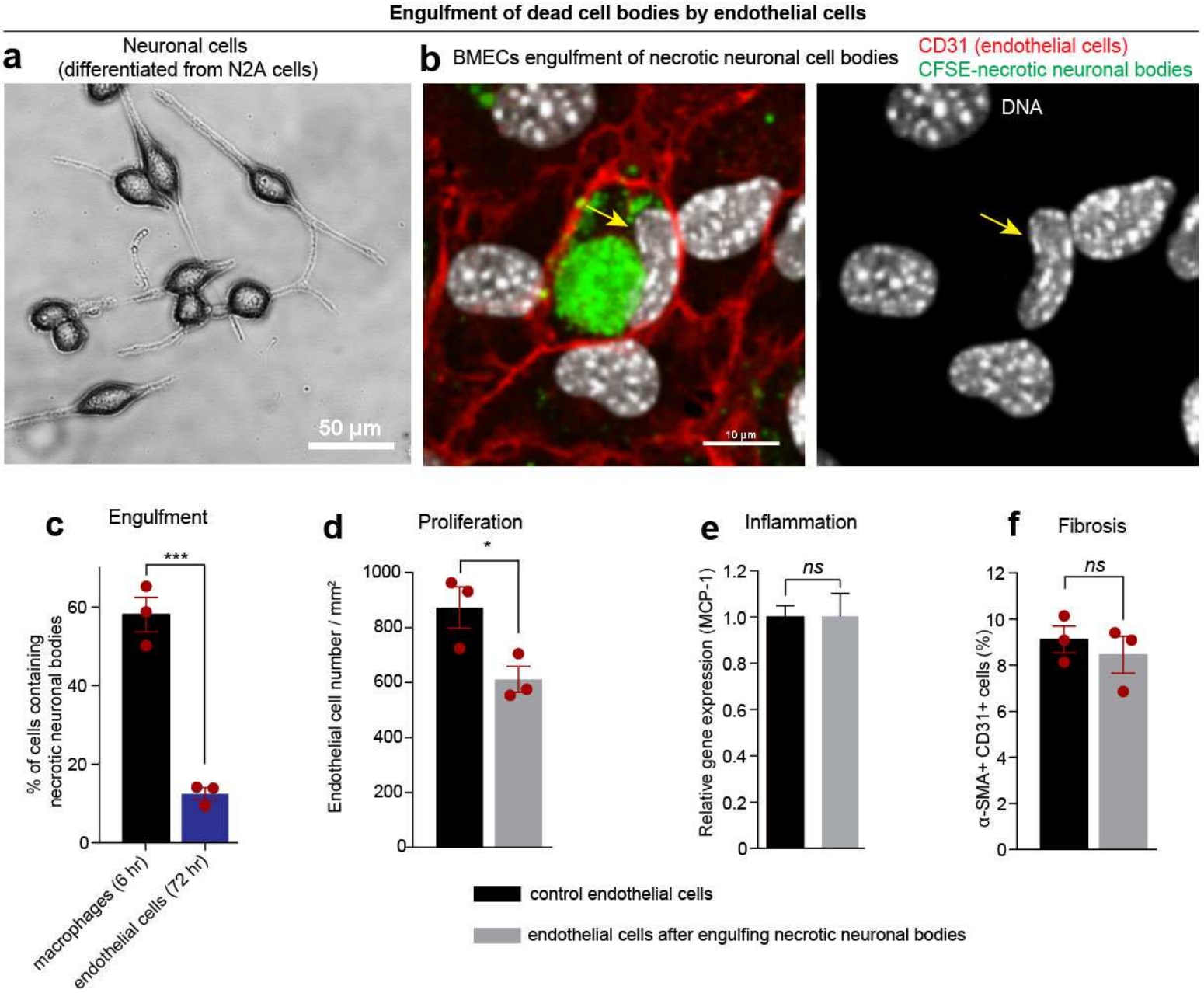

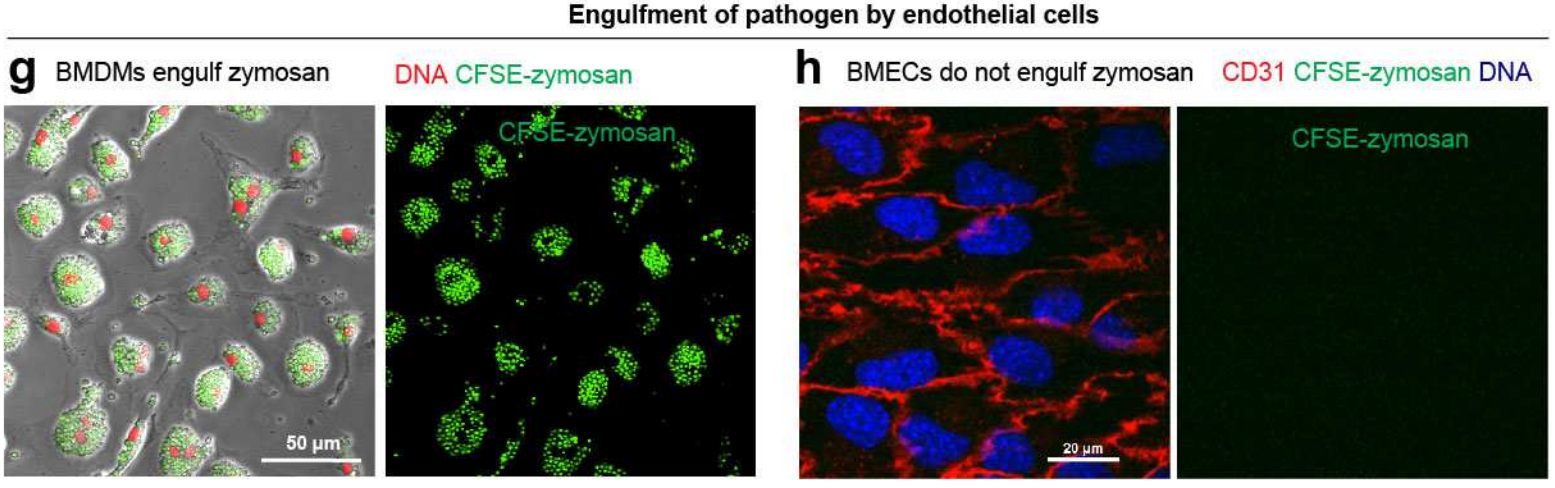

Supplemental figure 11.

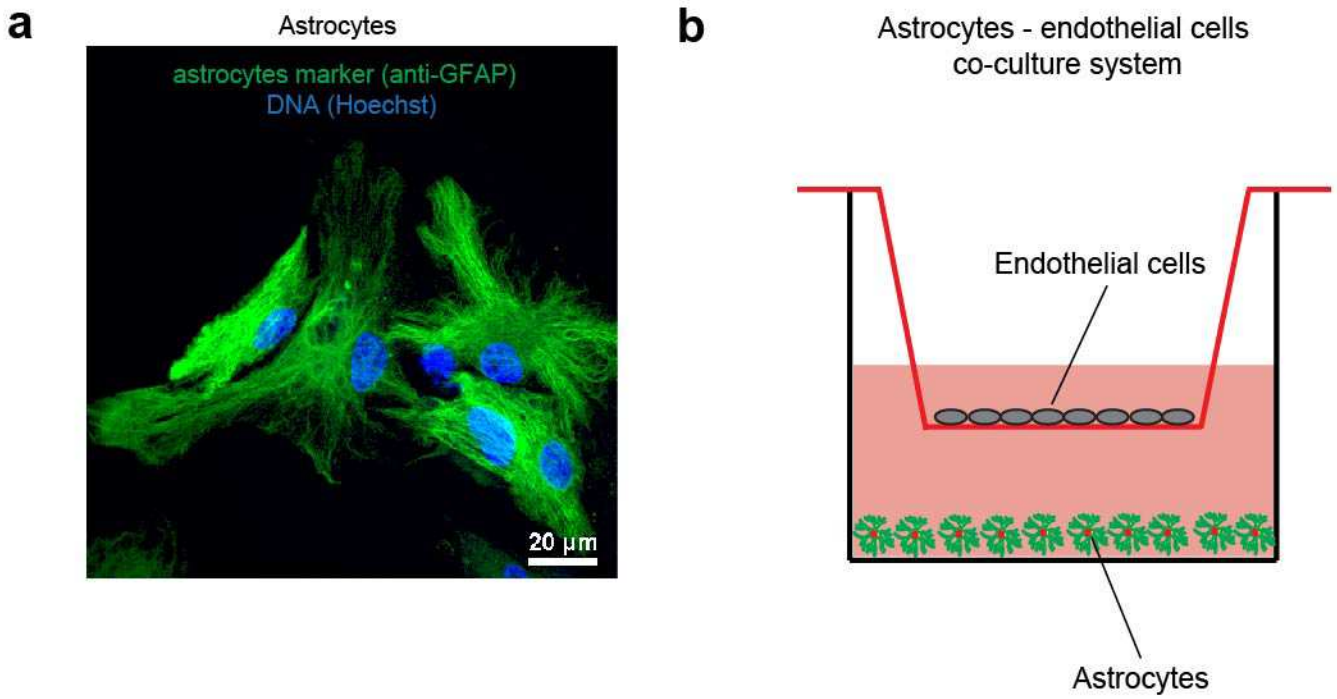

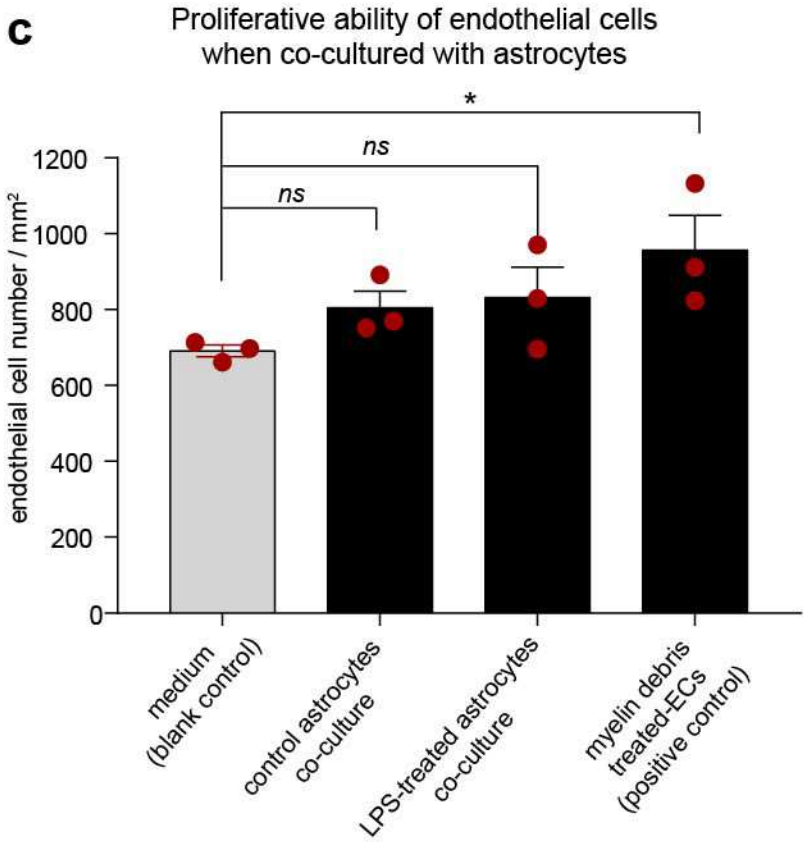

Supplemental figure 12.

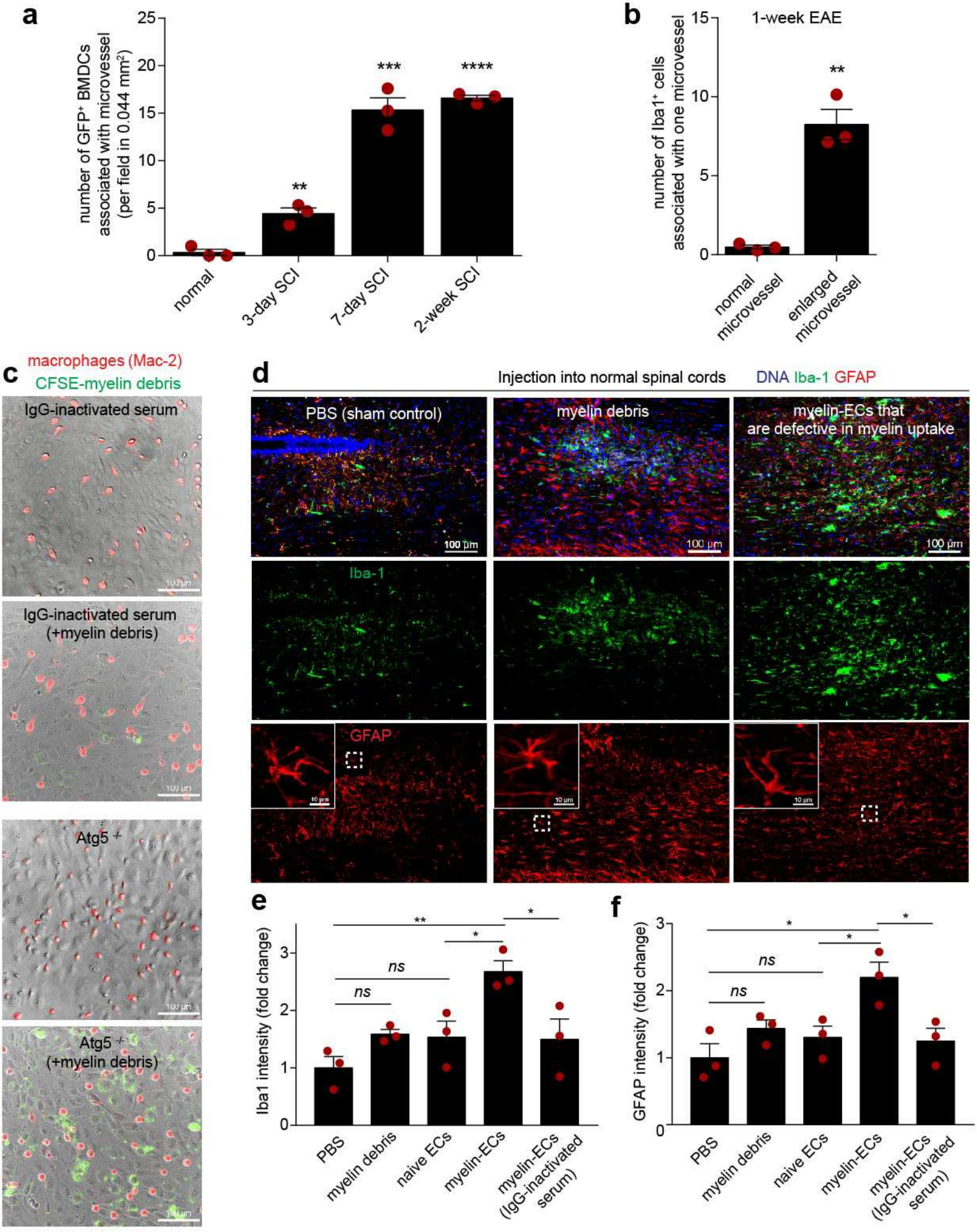

Supplemental figure 13.

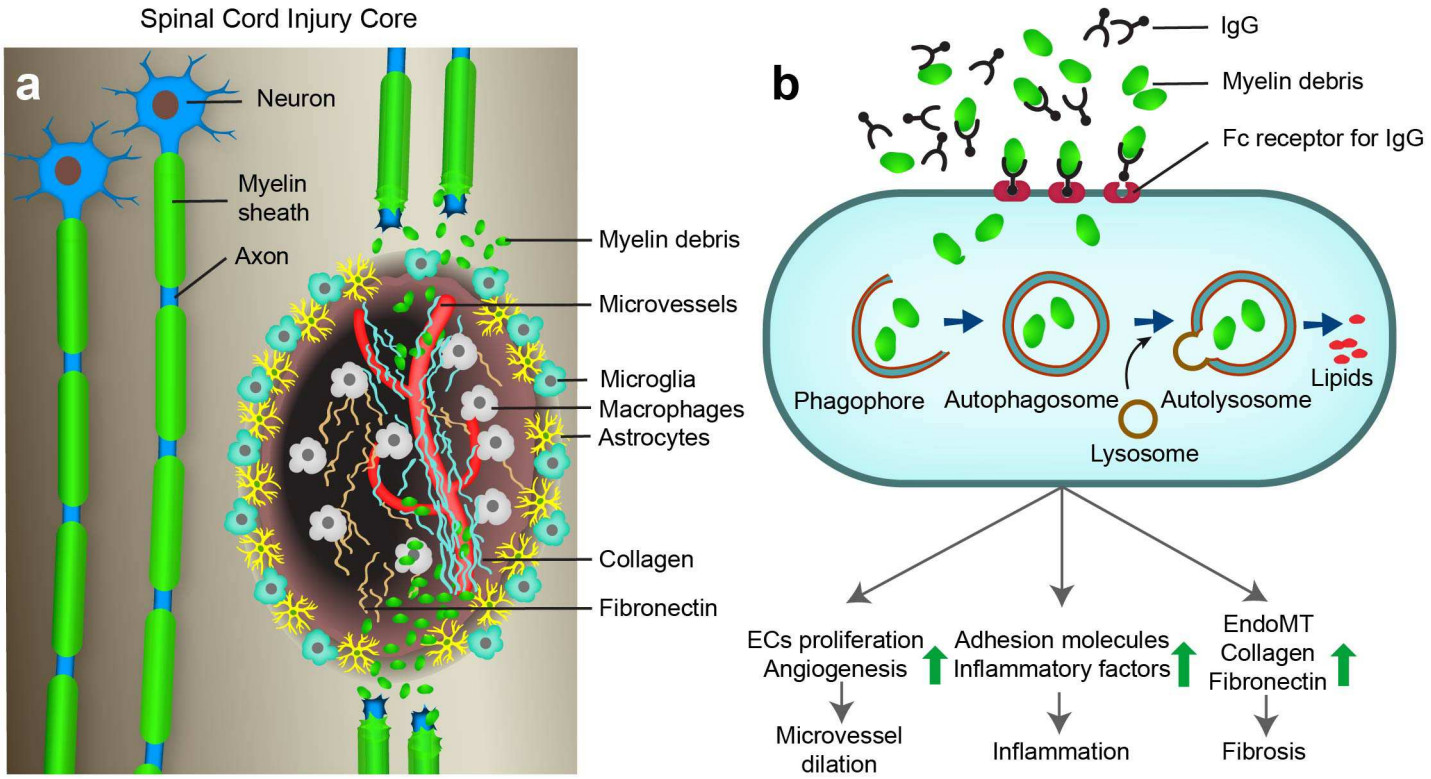

Supplemental figure 14.